Microglia regulate blood clearance in subarachnoid hemorrhage by heme oxygenase-1

Nils Schallner,[1,2] Rambhau Pandit,[3] Robert LeBlanc III,[3] Ajith J. Thomas,[1] Christopher S. Ogilvy,[1] Brian S. Zuckerbraun,[4] David Gallo,[1] Leo E. Otterbein,[1,5] and Khalid A. Hanafy[3]

[1]Department of Surgery, Beth Israel Deaconess Medical Center, Harvard Medical School, Boston, Massachusetts, USA. [2]Department of Anesthesiology and Intensive Care Medicine, University Medical Center Freiburg, Freiburg, Germany. [3]Department of Neurology, Beth Israel Deaconess Medical Center, Harvard Medical School, Boston, Massachusetts, USA. [4]Department of Surgery, University of Pittsburgh Medical Center, Pittsburgh, Pennsylvania, USA. [5]Aston University, Birmingham, United Kingdom.

Subarachnoid hemorrhage (SAH) carries a 50% mortality rate. The extravasated erythrocytes that surround the brain contain heme, which, when released from damaged red blood cells, functions as a potent danger molecule that induces sterile tissue injury and organ dysfunction. Free heme is metabolized by heme oxygenase (HO), resulting in the generation of carbon monoxide (CO), a bioactive gas with potent immunomodulatory capabilities. Here, using a murine model of SAH, we demonstrated that expression of the inducible HO isoform (HO-1, encoded by *Hmox1*) in microglia is necessary to attenuate neuronal cell death, vasospasm, impaired cognitive function, and clearance of cerebral blood burden. Initiation of CO inhalation after SAH rescued the absence of microglial HO-1 and reduced injury by enhancing erythrophagocytosis. Evaluation of correlative human data revealed that patients with SAH have markedly higher HO-1 activity in cerebrospinal fluid (CSF) compared with that in patients with unruptured cerebral aneurysms. Furthermore, cisternal hematoma volume correlated with HO-1 activity and cytokine expression in the CSF of these patients. Collectively, we found that microglial HO-1 and the generation of CO are essential for effective elimination of blood and heme after SAH that otherwise leads to neuronal injury and cognitive dysfunction. Administration of CO may have potential as a therapeutic modality in patients with ruptured cerebral aneurysms.

Introduction

Subarachnoid hemorrhage (SAH) leads to neuronal injury and cognitive impairment following heme-induced cerebral inflammation, which takes place in response to the accumulation of heme-containing blood components, particularly hemoglobin-saturated erythrocytes. The heme oxygenase (HO) enzymes are responsible for degrading heme into biliverdin, iron, and carbon monoxide (CO). There are 2 isoforms of HO: HO-1 is the ubiquitously expressed, inducible isoform, while HO-2 is constitutively expressed in the brain, endothelium, and testes. HO-1 is a cytoprotective molecule critical in maintaining cellular homeostasis and, when absent, results in exaggerated and unfettered inflammation. In contrast, induction of HO-1 exerts potent protective effects in numerous preclinical disease models including sepsis, trauma, vascular proliferative disease, acute lung and liver injury, and cancer (1–5). A number of recent reports have demonstrated the benefits of HO-1 in the CNS, including the eye (6) and brain (7–12). In the brain, expression of each HO isoform follows a distinct spatial and cell-specific distribution pattern. HO-2 is constitutively expressed in neuronal cells, and expression levels are not changed by stress such as ischemia or hemorrhagic injury (13, 14). In contrast, HO-1 is sparsely expressed in the uncompromised brain but strongly upregulated in glial cells following injury (13–19). A role for HO-1 in response to cerebral injury remains unclear but likely relates to the acute phase response and the generation of one or more of its bioactive products including CO, iron, and the bile pigments biliverdin and bilirubin. Exogenous application of low doses of CO can recapitulate the cytoprotective effects of HO-1 induction (20–28), but few studies have demonstrated that CO can actually substitute for the absence of HO-1 in a cell type–specific fashion, particularly in the brain. Only a few reports have examined the protective effects of CO on neuronal cells in vitro and in vivo (29–32). In fact, the majority of reports contend that CO is potently neurotoxic, resulting in memory loss, confusion, and even flu-like symptoms thought to arise in part from neuronal cell death. In direct contrast to this dogma, we provide compelling data demonstrating that CO can protect the brain, even when exposure is initiated after blood has accumulated within the subarachnoid space. The mechanism involves, in part, increased phagocytic activity of microglia to clear the erythrocyte burden. Moreover, when HO-1 is absent in microglia, there is impaired phagocytosis, increased neuronal injury, and cognitive dysfunction, all of which can be rescued with administration of CO.

Results

Pharmacological inhibition of HO leads to aggravated neuronal injury after SAH. We first characterized the role of HO in neuronal injury following SAH by pharmacologically blocking HO with tin protoporphyrin-IX (SnPP) in WT mice. We analyzed cerebral vaso-

---

Authorship note: Leo E. Otterbein and Khalid A. Hanafy contributed equally to this work.
Conflict of interest: The authors have declared that no conflict of interest exists.
Submitted: August 14, 2014; **Accepted:** April 27, 2015.
Reference information: *J Clin Invest.* 2015;125(7):2609–2625. doi:10.1172/JCI78443.

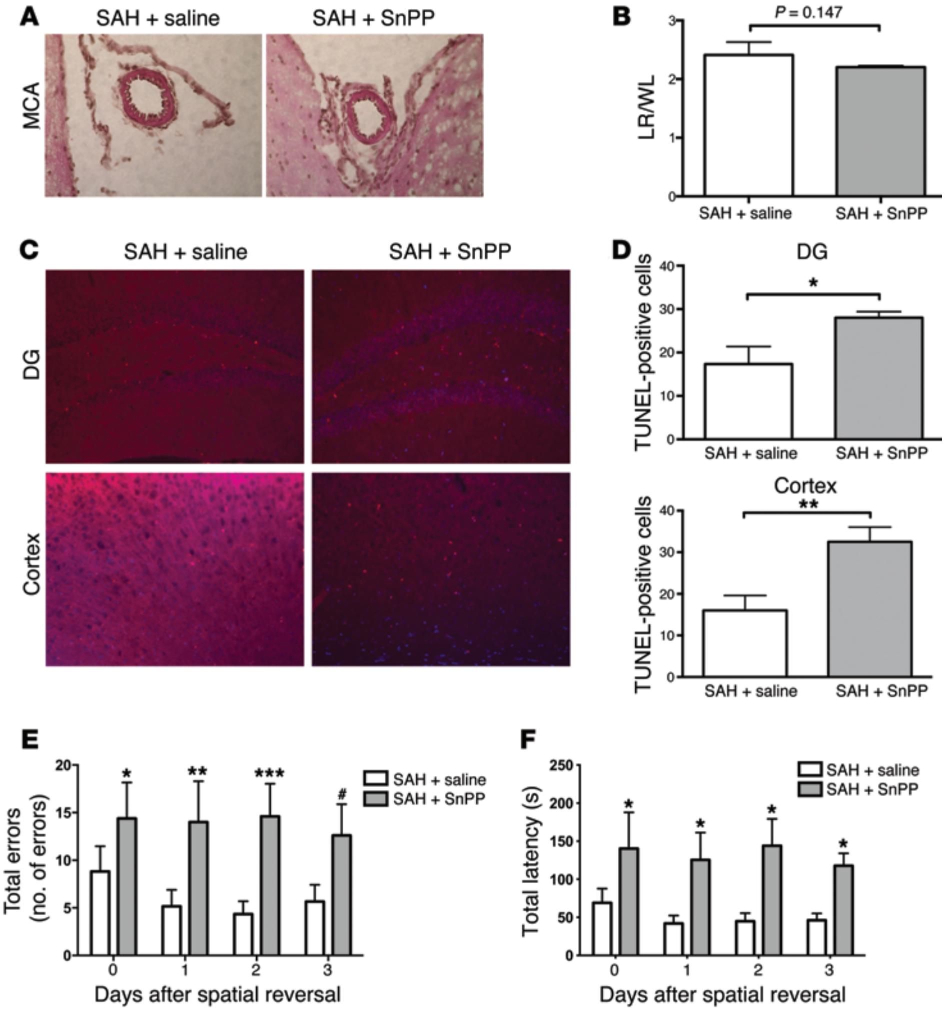

Figure 1. Aggravated neuronal injury after SAH due to HO inhibition with SnPP IX. (**A**) Representative ($n = 6$) H&E-stained cross sections of the MCA 7 days after SAH in animals treated with saline or the HO inhibitor SnPP (original magnification, ×40). (**B**) Quantification of MCA vasospasm, defined as the quotient of LR and WL. $P = 0.147$ for SAH plus saline versus SAH plus SnPP (2-tailed Student's *t* test; $n = 6$). (**C**) Representative images (original magnification, ×20; $n = 6$) from TUNEL staining (red) of the DG and cortex of mice that received SAH plus saline or SnPP treatment 7 days after injury. Nuclei were counterstained with Hoechst 33258 (blue). (**D**) Quantification of TUNEL-positive cells per microscopic field in the designated brain regions. $^{*}P = 0.0413$ (DG) and $^{**}P = 0.015$ (cortex) for SAH plus saline versus SAH plus SnPP (2-tailed Student's t test; $n = 6$). (**E**) Number of total errors in spatial memory function by Barnes maze assessment. Graph shows test results on the days after spatial reversal. $^{*}P = 0.0071$ (day 0), $^{**}P < 0.0001$ (day 1), $^{***}P < 0.0001$ (day 2), and $^{\#}P = 0.0007$ (day 3) for SAH plus saline versus SAH plus SnPP (2-way ANOVA; $n = 9$). (**F**) Total latency in seconds for spatial memory function testing by Barnes maze test. $^{*}P < 0.0001$ (days 0–3) for SAH plus saline versus SAH plus SnPP (2-way ANOVA; $n = 9$).

spasm, neuronal apoptosis, and cognitive function over a period of 7 days following SAH. WT mice subjected to SAH (WT SAH) treated with SnPP showed more severe vasospasm compared with WT SAH mice treated with vehicle (Figure 1, A and B). HO inhibition also significantly increased neuronal cell death in the dentate gyrus (DG) and cortex by 62% and 103%, respectively (Figure 1, C and D). Assessment of spatial memory function using the Barnes maze test showed that animals subjected to HO inhibition had an increased error rate, with greater delay in finding the goal box compared with controls (Figure 1, E and F). Importantly, no difference in task learning was observed prior to SAH (Supplemental Figure 1, A and B; supplemental material available online with this article; doi:10.1172/JCI78443DS1).

SAH-induced neuronal injury and the role of HO-1 in microglia. SnPP administration inhibited both HO-1 and HO-2 globally and therein carries some degree of nonspecificity. We therefore used a more rigorous genetic approach to specifically test the importance of HO-1 in response to SAH. Since HO-1 is primarily upregulated in microglia following neuronal injury (13, 14, 16), we generated *LyzM-Cre Hmox1*$^{fl/fl}$ mice, in which HO-1 is specifically deleted in cells expressing lysozyme, including microglia (Figure 2). After confirming the absence of HO-1 in cultured primary microglia isolated from *LyzM-Cre Hmox1*$^{fl/fl}$, but not in microglia from *Hmox1*$^{fl/fl}$ control mice (Figure 2, A and B), cohorts of *LyzM-Cre Hmox1*$^{fl/fl}$ and *Hmox1*$^{fl/fl}$ mice were subjected to SAH, as described above. As was observed with pharmacologic inhibition, *LyzM-Cre Hmox1*$^{fl/fl}$ mice showed significantly increased vasospasm and neuronal apoptosis compared with *Hmox1*$^{fl/fl}$ control mice after SAH, which corresponded with significantly impaired cognitive function in the Barnes maze test (Figure 2, C–H). Again, no difference in task learning was observed prior to SAH (Supplemental Figure 1, C and D).

LyzM-Cre Hmox1$^{fl/fl}$ mice express Cre recombinase in all cells of myeloid lineage. Therefore, to distinguish between the role of HO-1 in brain-resident microglia versus peripheral myeloid cells that might infiltrate the brain following SAH and contribute to the effects seen, we transplanted BM from HO-1–competent animals into *LyzM-Cre Hmox1*$^{fl/fl}$ mice prior to SAH. The requisite total-body irradiation necessary to reconstitute BM compromises the blood-brain barrier (BBB) and permits infiltration of peripheral leukocytes (33). Using a lead helmet and transplanting BM from *Cx3cr1-GFP* mice, we observed no leukocyte infiltration into the brain after irradiation compared with transplanted animals irradiated without the lead helmet (Supplemental Figure 2). We concluded that head shielding prevented BBB compromise. This methodology thus enabled us to generate chimeric mice containing peripheral HO-1–competent myeloid lineage cells, while simul-

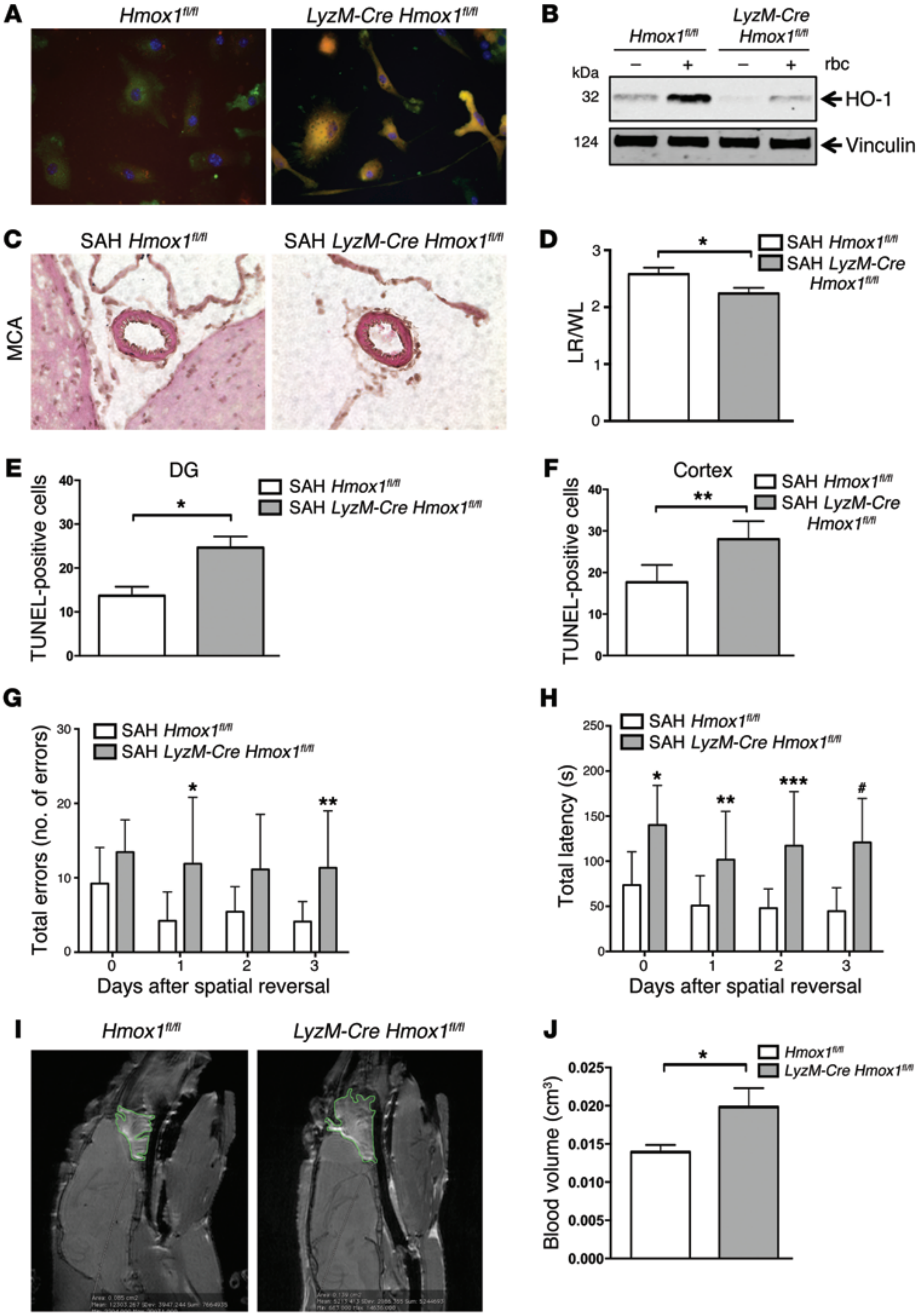

Figure 2. Role of microglial HO-1 in neuronal injury after SAH. (**A**) PMG isolated from brains of *Hmox1*$^{fl/fl}$ or *LyzM-Cre Hmox1*$^{fl/fl}$ mice stained for IBA1 (green) and nuclear counterstaining with Hoechst 33258 (blue). DsRed expression (red; yellow for red/green merged) was exclusively initiated when the LoxP site–flanked *Hmox1* gene was deleted in cells with *LyzM-Cre* gene expression (right panel, original magnification, ×40; $n = 3$). (**B**) HO-1 protein analyzed by Western blotting in PMG from brains of *Hmox1*$^{fl/fl}$ control or *LyzM-Cre Hmox1*$^{fl/fl}$ mice with or without red blood cell exposure ($n = 3$). (**C**) Representative ($n = 6$) H&E-stained cross sections of the MCA after SAH in *Hmox1*$^{fl/fl}$ and *LyzM-Cre Hmox1*$^{fl/fl}$ mice (original magnification, ×40). (**D**) Quantification of MCA vasospasm, defined as the quotient of LR and WL. $^*P = 0.018$ (2-tailed Student's *t* test; $n = 6$). (**E** and **F**) Quantification of TUNEL-positive cells per microscopic field in the DG (**E**) and cortex (**F**). $^*P = 0.0043$ (**E**) and $^{**}P = 0.0412$ (**F**) (2-tailed Student's *t* test; $n = 6$). (**G**) Number of total errors in spatial memory function by Barnes maze assessment. $^*P = 0.0071$ (day 1) and $^{**}P = 0.0123$ (day 3) (2-way ANOVA; $n = 9$). (**H**) Total latency in seconds for spatial memory function by Barnes maze assessment. $^*P = 0.0033$ (day 0), $^{**}P = 0.0345$ (day 1), $^{***}P = 0.0021$ (day 2), and $^{\#}P = 0.0006$ (day 3) (2-way ANOVA; $n = 9$). (**I**) Representative MR images ($n = 3$) of mice with intracranial injection of gadopentetate dimeglumine–labeled blood. (**J**) Quantification of radiographically assessed hematoma volume. $^*P = 0.0184$ (2-tailed Student's *t* test; $n = 3$).

taneously maintaining HO-1–deficient microglia. Importantly, head shielding not only prevented cerebral leukocyte infiltration before SAH, but also after SAH (Figure 3, A and B), indicating that infiltration of peripheral myeloid cells into the brain is likely not directly involved in SAH-induced neuronal inflammation and injury, although further quantitative experiments are required.

Using the methodology described above, we next transplanted BM from HO-1–competent animals (*MY-Hmox1*$^{+/+}$) into irradiated *LyzM-Cre Hmox1*$^{fl/fl}$ (*MG-Hmox1*$^{-/-}$) and *Hmox1*$^{fl/fl}$ (*MG-Hmox1*$^{+/+}$) control mice with head shielding and subjected them to SAH 1 month after BM transplant. One week after SAH, *LyzM-Cre Hmox1*$^{fl/fl}$ chimeras (*MG-Hmox1*$^{-/-}$ *MY-Hmox1*$^{+/+}$) showed a significantly greater vasospasm response and neuronal apoptosis with spatial memory function impairment compared with that seen in control chimeric mice (*MG-Hmox1*$^{+/+}$ *MY-Hmox1*$^{+/+}$) (Figure 3, C–H). On the basis of these results, we concluded that the phenotype observed in *LyzM-Cre Hmox1*$^{fl/fl}$ mice was principally due to HO-1 deficiency in microglia and that HO-1 expression in peripheral cells of the myeloid lineage contribute little to SAH-induced injury.

We next tested whether HO-1 expression in any other glial cells of the brain participated in SAH-induced injury. Mice with neuron- and astrocyte-specific HO-1 deletion (*Nes-Cre Hmox1*$^{fl/fl}$), unlike *LyzM-Cre Hmox1*$^{fl/fl}$ mice, did not display increased neu-

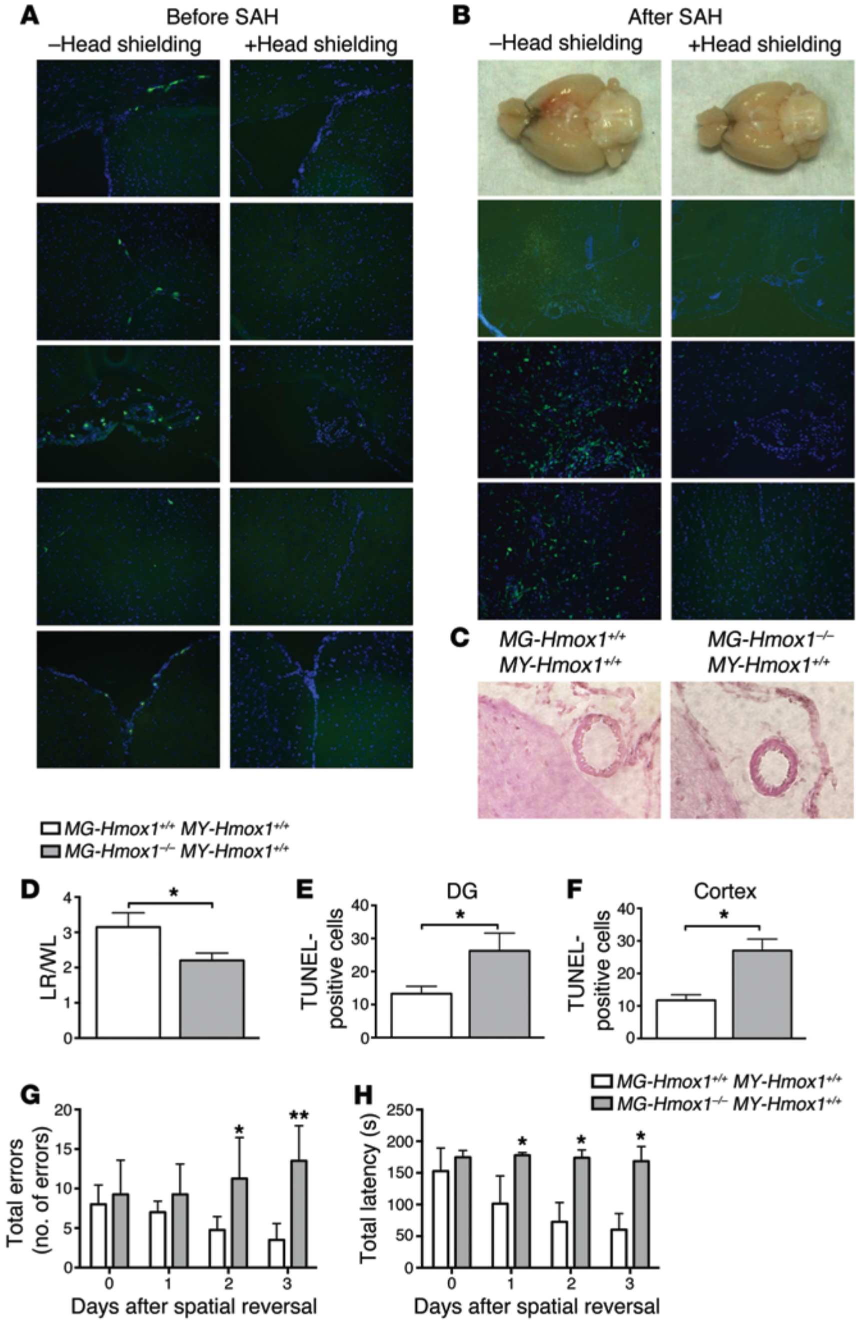

Figure 3. HO-1–competent BMTx does not influence neuronal injury after SAH in mice deficient in microglial HO-1. (**A**) Representative ($n = 6$) brain tissue sections (original magnification, ×20) depicting the prevention of BM-derived cell engraftment into the brain 4 weeks after whole-body irradiation (12 Gy) and transplantation of BM cells from *Cx3cr1-GFP* mice by lead shielding of the head (see Supplemental Figure 1). (**B**) Representative ($n = 6$) macroscopic views and microscopic brain tissue sections illustrating that head shielding during radiation prevents infiltration of BM-derived *Cx3cr1-GFP* cells into the brain 7 days after SAH. Original magnification, ×4 (2nd row of panels from top) and ×20 (bottom 4 panels). (**C**) Representative ($n = 6$) H&E-stained cross sections (original magnification, ×40) of the MCA after SAH in *LyzM-Cre Hmox1*$^{fl/fl}$ chimeras (*MG-Hmox1*$^{-/-}$ *MY-Hmox1*$^{+/+}$) and control chimeric mice (*MG-Hmox1*$^{+/+}$ *MY-Hmox1*$^{+/+}$). (**D**) Quantification of MCA vasospasm. $^{*}P = 0.0059$ (2-tailed Student's *t* test; $n = 6$). (**E** and **F**) Quantification of TUNEL-positive cells per microscopic field in the DG (**E**) and cortex (**F**). $^{*}P = 0.0042$ (DG) and $P = 0.0002$ (cortex) (2-tailed Student's *t* test; $n = 6$). (**G**) Number of total errors in spatial memory function by Barnes maze assessment. $^{*}P = 0.0294$ (day 2) and $^{**}P = 0.0005$ (day 3) (2-way ANOVA; $n = 6$). (**H**) Total latency in seconds for spatial memory function by Barnes maze assessment. $^{*}P < 0.0001$ for days 1–3 (by 2-way ANOVA; $n = 6$).

ronal injury or memory impairment compared with *Hmox1*$^{fl/fl}$ control mice (Figure 4). Therefore, we concluded that HO-1 expression in astrocytes and neurons was not involved in neuronal injury or cognitive impairment after SAH.

With evidence that microglial HO-1 was critical in mediating cerebral inflammation after SAH, we next tested whether HO-1 was involved in clearance of the blood burden after SAH. MRI showed 42% greater hematoma volumes in *LyzM-Cre-Hmox1*$^{fl/fl}$ mice compared with those in *Hmox1*$^{fl/fl}$ control mice (Figure 2, I and J). Collectively, these data demonstrate that HO-1 in microglia is necessary to eliminate blood and defend against blood-induced injury and the development of neurocognitive deficits.

Hematoma volume in aneurysmal SAH patients correlates with HO-1 expression. With a role for microglial HO-1 established in our mouse model of SAH, we next investigated the role of HO-1 in patients with aneurysmal SAH. We enrolled 11 patients with SAH (Figure 5A) and measured HO-1 expression over time in both the cerebrospinal fluid (CSF) and peripheral blood. We observed a time-dependent increase in HO-1 expression in the CSF, peaking 7 days after rupture, that was not observed in patients with unruptured cerebral aneurysms. HO-1 expression correlated with the amount of cisternal hematoma volume (CHV), as well as CSF bilirubin levels, an indirect marker of HO catalytic activity (Figure 5, B–E). HO-1 expression in peripheral blood leukocytes of SAH patients showed different kinetics, with peak expression occurring on day 1 versus controls and expression remaining elevated through day 7 (Figure 5F). We further investigated inflammatory markers in the CSF of SAH patients and found a sustained ele-

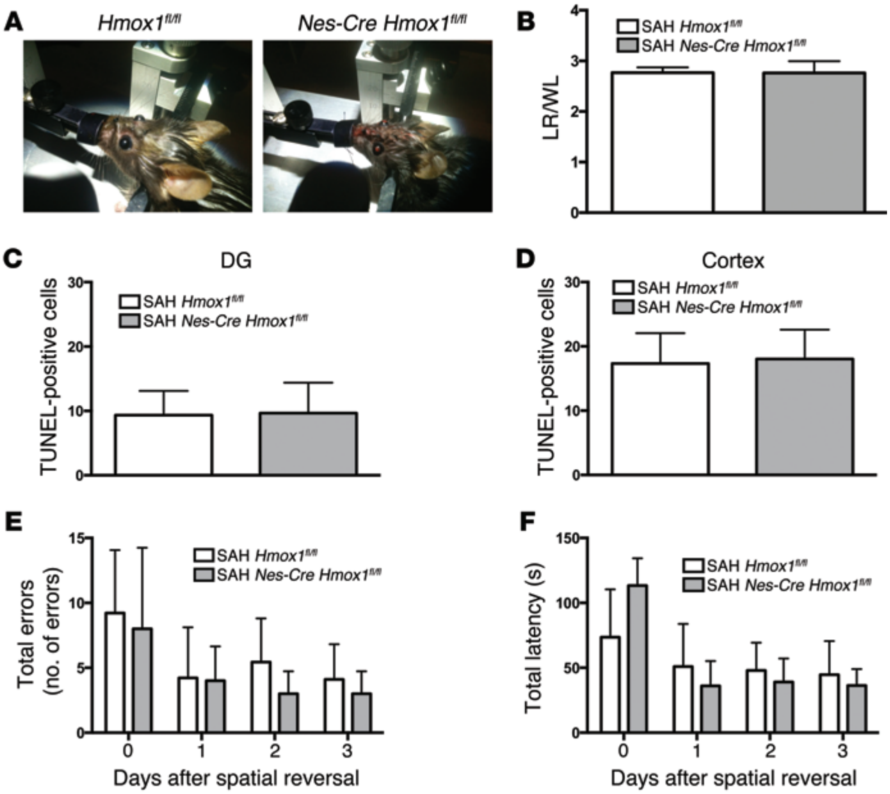

Figure 4. HO-1 deficiency in neurons and astrocytes does not influence neuronal injury after SAH. (**A**) Animals with neuron- and astrocyte-specific HO-1 deficiency (*Nes-Cre Hmox1$^{fl/fl}$*, right panel) showed visible DsRed expression in retinal neurons compared with controls (*Hmox1$^{fl/fl}$*, left panel, representative of 6 mice). DsRed expression was exclusively initiated when the LoxP site–flanked *Hmox1* gene was deleted in cells with *Nes-Cre* gene expression. (**B**) Quantification of MCA vasospasm, defined as the quotient of LR and WL. *P* = NS (2-tailed Student's *t* test; *n* = 6). (**C** and **D**) Quantification of TUNEL-positive cells per microscopic field in the DG (**C**) and cortex (**D**). *P* = NS (2-tailed Student's *t* test; *n* = 6). (**E**) Number of total errors in spatial memory function by Barnes maze assessment. Graph shows test results on the days after spatial reversal. *P* = NS (2-way ANOVA; *n* = 9). (**F**) Total latency in seconds for spatial memory function by Barnes maze assessment. *P* = NS (2-way ANOVA (*n* = 9).

vation of proinflammatory cytokines including IL-1β, IL-8, and TNF-α, but also elevated antiinflammatory IL-10 (Figure 5, G–K). Collectively, these data show that sudden accumulation of blood into the subarachnoid space in the brain results in an elevation of HO-1 expression in the CSF of patients and thus may be an important response mechanism in hemorrhage-induced inflammation and neuronal cell death.

HO-1 expression in microglia is important in erythrophagocytosis and neuroprotection. Given the MRI results for the *LyzM-Cre Hmox1$^{fl/fl}$* mice with SAH compared with those for *Hmox1$^{fl/fl}$* controls, we surmised that a role for microglial HO-1 in hematoma resolution could exist. We hypothesized that erythrophagocytosis by microglia required in part HO-1, was critical to neuronal survival, and explained in part the cognitive dysfunction in mice lacking microglial HO-1. To study this, we isolated primary microglia (PMG) from *LyzM-Cre Hmox1$^{fl/fl}$* mice and *Hmox1$^{fl/fl}$* control animals, exposed them to fluorescence-labeled red blood cells, and analyzed phagocytosis of red blood cells by flow cytometry and light microscopy. Compared with PMG from *Hmox1$^{fl/fl}$* mice, *LyzM-Cre Hmox1$^{fl/fl}$* PMG showed less phagocytic activity (Figure 6A). The mean fluorescence per cell, indicative of the number of red blood cells phagocytosed per microglia, was 36% lower in microglia from *LyzM-Cre Hmox1$^{fl/fl}$* mice than in microglia from control animals (Figure 6B). We also analyzed erythrophagocytosis by light microscopy for visual confirmation of the flow cytometric data. The number of red blood cells per PMG and the percentage of red blood cell–positive PMG were significantly reduced in microglia from *LyzM-Cre Hmox1$^{fl/fl}$* mice (Figure 6, C–E).

On the basis of the results described above, we next tested whether the impaired phagocytosis observed in *LyzM-Cre Hmox1$^{fl/fl}$* PMG was involved in neuronal apoptosis in response to red blood cells. Indeed, when HT22 neuronal cells were cocultured with red blood cell–treated microglia from *LyzM-Cre Hmox1$^{fl/fl}$* mice, neuronal apoptosis measured by TUNEL was significantly increased compared with that seen in *Hmox1$^{fl/fl}$* control PMG (Figure 6, F and G). To confirm that this increase in neuronal apoptosis was due to impaired red blood cell phagocytosis, we blocked phagocytosis pharmacologically in WT PMG and assessed the amount of neuronal apoptosis by TUNEL staining. Two different phagocytosis inhibitors (cytochalasin D and dynasore) significantly increased neuronal cell death in response to red blood cell treatment (Figure 6H). This impairment of red blood cell phagocytosis in WT PMG in the presence of the phagocytosis inhibitors, as well as in PMG from *LyzM-Cre Hmox1$^{fl/fl}$* mice, was also observed by light microscopy (data not shown).

CO modulates neuronal injury after SAH by enhancing clearance of blood and modulating inflammation. After defining the protective role of HO-1 in SAH, we next sought to evaluate whether the protective effect of HO-1 could be mimicked by exogenous application of CO, one of its catalytic products. We first analyzed the effect of CO exposure on WT mice subjected to SAH and evaluated vasospasm, neuronal apoptosis, and memory function after SAH with or without CO. CO gas exposure was started 1 hour after SAH and then repeated daily for the duration of the experiment. Animals treated with CO showed significantly decreased vasospasm and neuronal apoptosis in the hippocampus and cortex (Figure 7, A–D). Spatial memory function was significantly improved after spatial reversal in animals treated with CO compared with those exposed to room air (RA) in 2 separate spatial memory tests (Figure 7, E–G). Finally, hematoma volume measured by MRI in mice

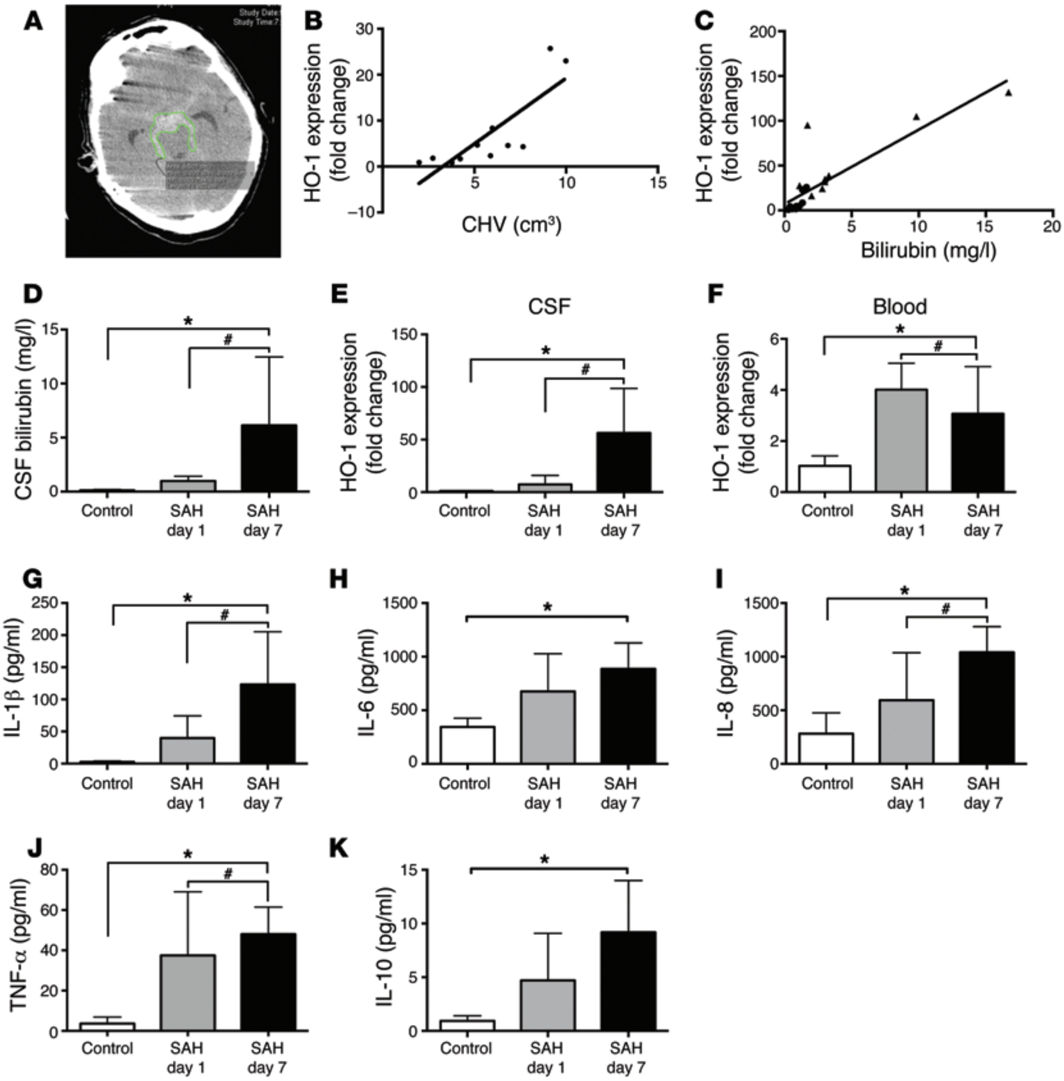

Figure 5. HO-1 expression and activity are determined by hematoma volume in human SAH patients. (**A**) Representative (n = 11) CT scan of SAH patient obtained within 24 hours of admission. (**B**) Spearman's correlation of CSF cellular HO-1 expression of SAH patients (n = 11) versus CHV on day 1. r = 0.84 (95% CI: 0.46–0.96); P = 0.0022. (**C**) Spearman's correlation for HO-1 expression on day 1 (circles) and day 7 (triangles) versus CSF bilirubin content. r = 0.92 (95% CI: 0.80–0.97); $P < 0.0001$. (**D**) CSF bilirubin content for SAH patients versus control patients (unruptured cerebral aneurysm). *P = 0.0157 for day-7 SAH versus control and #P = 0.0123 for day-7 SAH versus day-1 SAH (1-way ANOVA; n = 11). (**E**) CSF cellular HO-1 expression after SAH versus controls. *P = 0.0029 for day-7 SAH versus control and #P = 0.0012 for day-1 SAH versus control (1-way ANOVA; n = 11). (**F**) HO-1 expression in peripheral blood leukocytes after SAH versus controls. *P = 0.0002 for control versus day-1 SAH and #P = 0.0122 for day-1 SAH versus day-7 SAH (1-way ANOVA; n = 11). (**G**–**K**) IL-1β (**G**; *P = 0.0016 for control versus day-7 SAH and #P = 0.0067 for day-1 SAH versus day-7 SAH); IL-6 (**H**; *P = 0.0123 for control versus day-7 SAH); IL-8 (**I**; *P = 0.0045 for control versus day-7 SAH and #P = 0.0459 for day-1 SAH versus day-7 SAH); TNF-α (**J**; *P = 0.0451 for control versus day-1 SAH and #P = 0.0144 for control versus day-7 SAH); and IL-10 (**K**; *P = 0.0072 for control versus day-7 SAH) concentrations in CSF compared with controls (all by 1-way ANOVA; n = 11).

treated with CO after SAH was significantly reduced compared with that in animals treated with RA (Figure 7, H and I).

To establish that the effects seen with gaseous CO were not specific to the route of delivery, we administered a CO-releasing molecule (CO-RM). Intravenous injection of CO-saturated, pegylated hemoglobin (MP4CO) had beneficial effects in the brain similar to those observed with inhaled CO when compared with control pegylated hemoglobin without CO (Figure 8, A–D).

As sex-specific treatment effects have been observed in various brain injury models (34), we also evaluated the effects of CO on female mice in our SAH model and found a protective effect of CO on vasospasm and neuronal apoptosis comparable to that seen in male WT mice (Figure 8, E–H).

CO is a potent antiinflammatory molecule (28). We next tested whether CO influenced SAH-induced neuroinflammation, as assessed by expression of the astrocytic and microglial activation markers GFAP and IBA1, respectively. CO increased IBA1 expression in SAH mice at the base of the brain and cortex compared with that detected in SAH mice exposed to RA (Figure 9A), while GFAP reactivity was reduced in all brain regions in SAH animals treated with CO (Figure 9B). Microglial activation assessed by morphology was altered by SAH, with loss of ramification and thickening of pro-

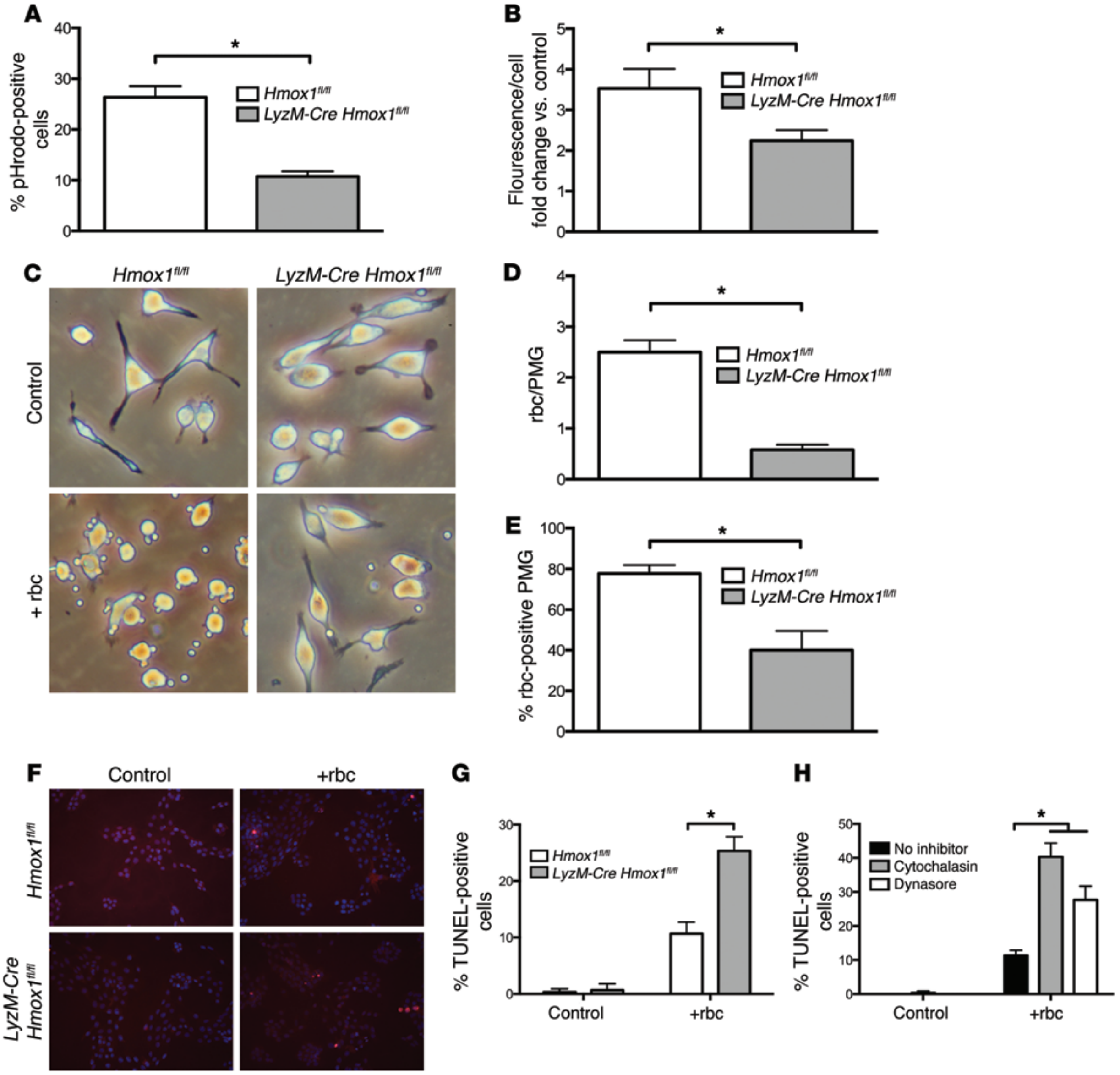

Figure 6. Importance of microglial HO-1 for erythrophagocytosis and neuronal survival in vitro. (**A**) Quantification of the percentage of microglia positive for fluorescence-labeled (pHrodo) red blood cells by flow cytometric analysis. $^*P = 0.0015$ for *Hmox1*$^{fl/fl}$ red blood cells versus *LyzM-Cre Hmox1*$^{fl/fl}$ red blood cells (2-tailed Student's *t* test; $n = 3$). (**B**) Mean fluorescent signal in microglia after exposure to fluorescence-labeled red blood cells. $^*P = 0.0274$ for *Hmox1*$^{fl/fl}$ red blood cells versus *LyzM-Cre Hmox1*$^{fl/fl}$ red blood cells (2-tailed Student's *t* test; $n = 3$). (**C**) Representative ($n = 3$) light microscopic images (original magnification, ×40) of *Hmox1*$^{fl/fl}$ and *LyzM-Cre Hmox1*$^{fl/fl}$ microglia after exposure to red blood cells. (**D**) Quantification of red blood cells per microglia, analyzed by light microscopy. $^*P < 0.0001$ for *Hmox1*$^{fl/fl}$ red blood cells versus *LyzM-Cre Hmox1*$^{fl/fl}$ red blood cells (2-tailed Student's *t* test; $n = 3$). (**E**) Quantification of the percentage of red blood cell–positive microglia by light microscopy. $^*P < 0.0001$ for *Hmox1*$^{fl/fl}$ red blood cells versus *LyzM-Cre Hmox1*$^{fl/fl}$ red blood cells (2-tailed Student's *t* test; $n = 3$). (**F**) Representative images (original magnification, ×20; $n = 3$) from TUNEL staining (red) of neuronal cells cocultured with *Hmox1*$^{fl/fl}$ or *LyzM-Cre Hmox1*$^{fl/fl}$ microglia with or without red blood cells. Cell nuclei were counterstained with Hoechst 33258 (blue). (**G**) Quantification of TUNEL-positive neuronal cells per microscopic view. $^*P < 0.0001$ for *Hmox1*$^{fl/fl}$ red blood cells versus *LyzM-Cre Hmox1*$^{fl/fl}$ red blood cells (2-tailed Student's *t* test; $n = 3$). (**H**) Quantification of TUNEL-positive neuronal cells per microscopic view. Neuronal cells were cocultured with WT PMG treated with the indicated pharmacological inhibitors of phagocytosis. $^*P < 0.0001$ for red blood cells without inhibitor versus red blood cells plus cytochalasin and versus red blood cells plus dynasore (1-way ANOVA; $n = 3$).

cesses, and was unchanged in the presence of CO or RA compared with naive controls (Figure 9C). These data demonstrate that similar to the in vitro studies, CO enhances hematoma clearance and modulates neuroinflammation in vivo and does so irrespective of sex.

HO-1 deficiency can be rescued with inhaled CO. After showing that CO was effective in reducing neuronal injury after SAH, we next asked whether exogenous application of CO could recapitulate the neuroprotective effects in microglia lacking HO-1 in vivo. We exposed animals treated with SnPP, as well as cohorts of *LyzM-Cre Hmox1*$^{fl/fl}$ mice, to CO (250 ppm) following SAH. SnPP-injected SAH mice treated with CO showed less vasospasm and neuronal apoptosis than did animals injected with SnPP alone

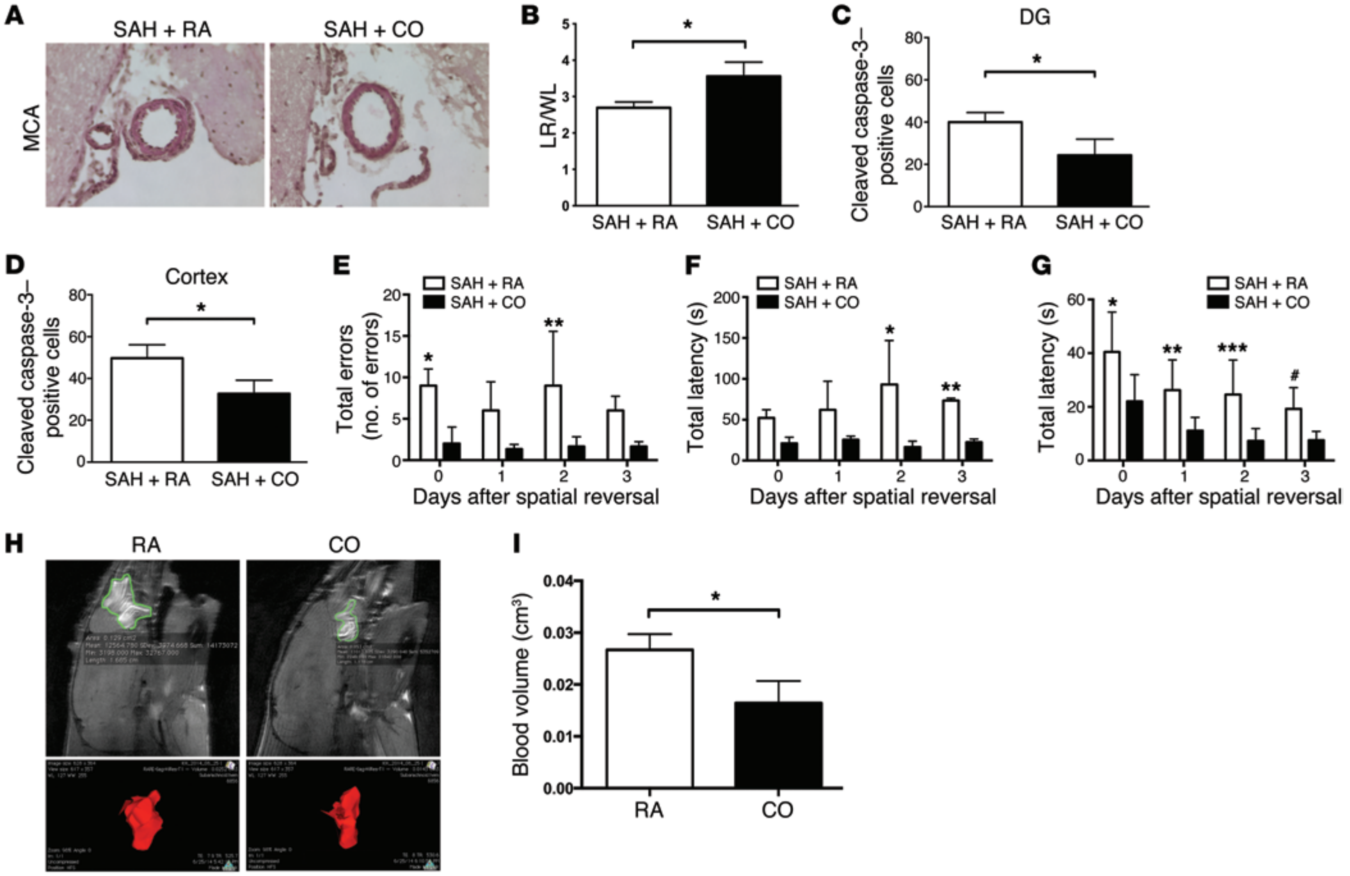

Figure 7. Exogenous CO gas treatment reduces neuronal injury after SAH in WT mice. (**A**) Representative (*n* = 6) H&E-stained cross sections (original magnification, ×40) of the MCA 7 days after SAH in WT mice treated with RA or CO. (**B**) Quantification of MCA vasospasm, defined as the quotient of LR and WL. **P* = 0.024 for SAH plus RA versus SAH plus CO (2-tailed Student's *t* test; *n* = 6). (**C** and **D**) Quantification of cleaved caspase-3–positive cells per microscopic view in the DG (**C**; **P* = 0.0382) and cortex (**D**; **P* = 0.0323) for SAH plus RA versus SAH plus CO (2-tailed Student's *t* test; *n* = 6). (**E**) Number of total errors in spatial memory function by Barnes maze assessment. Graphs show test results on the days after spatial reversal. **P* = 0.022 (day 0) for SAH plus RA versus SAH plus CO and ***P* = 0.0155 (day 2) (2-way ANOVA; *n* = 9). (**F**) Total latency in seconds for spatial memory function by Barnes maze assessment. **P* = 0.0014 (day 2) and ***P* = 0.0417 (day 3) (2-way ANOVA; *n* = 9). (**G**) Total latency in seconds for spatial memory function by Morris water maze assessment. **P* = 0.0005 (day 0); ***P* = 0.0054 (day 1); ****P* = 0.0012 (day 2); and $^{\#}$*P* = 0.0479 (day 3) (2-way ANOVA; *n* = 9). (**H**) Representative (*n* = 3) MRIs of mice with intracranial injection of gadopentetate dimeglumine–labeled blood with or without CO treatment. (**I**) Quantification of radiographically assessed hematoma volume in mice treated with RA or CO. **P* = 0.0277 (2-tailed Student's *t* test; *n* = 3).

(Figure 10, A–C). Similar rescue effects of CO on vasospasm and apoptosis were also observed in *LyzM-Cre Hmox1*$^{fl/fl}$ mice compared with *Hmox1*$^{fl/fl}$ controls (Figure 10, D–F). Importantly, CO was able to reverse the loss in spatial memory observed in SnPP-treated and *LyzM-Cre Hmox1*$^{fl/fl}$ mice (Figure 10, G–J). On the basis of these results, we concluded that CO generation was a critical neuroprotective product of heme metabolism and that the ability of microglia to generate CO was necessary for effective blood clearance and therein a reduction in neuronal injury after SAH. Importantly, these data suggest that exogenous CO can in part recapitulate the endogenous protective effects of HOs after SAH.

CO enhances microglial erythrophagocytosis to prevent neuronal apoptosis. To further corroborate the in vivo findings, we next studied the effect of CO exposure on erythrophagocytosis in the presence and absence of HO-1 in PMG in vitro. PMG were loaded with pHrodo Green, which measures phagocytosis by a pH-dependent fluorescent signal. PMG were exposed to fresh erythrocytes, and changes in the pHrodo signal were measured over time by flow cytometry and visual counting. The impaired erythrophagocytosis observed in PMG from *LyzM-Cre Hmox1*$^{fl/fl}$ mice compared with that in control PMG was rescued when cells were exposed to CO (Figure 11, A–E). As a consequence of these observations of phagocytosis, we next hypothesized that the ability of the PMG to phagocytose erythrocytes would dictate the susceptibility of neurons to red blood cell–induced cell death. In Transwell experiments, *LyzM-Cre Hmox1*$^{fl/fl}$ PMG were cocultured with HT22 neuronal cells. Fresh erythrocytes were added to the PMG, and neuronal cell death was measured by TUNEL staining. Lack of HO-1 in PMG resulted in enhanced neuronal cell death, which could be rescued with CO exposure (Figure 11, F and G). We concluded from these data that PMG become activated by exposure to erythrocytes and secrete mediators that in turn cause neuronal apoptosis. The protective effects of CO in this setting may be explained by an increased phagocytic ability of PMG and possibly a reduction in factors that induce neuronal apoptosis. Alternatively, CO may directly affect neuronal survival.

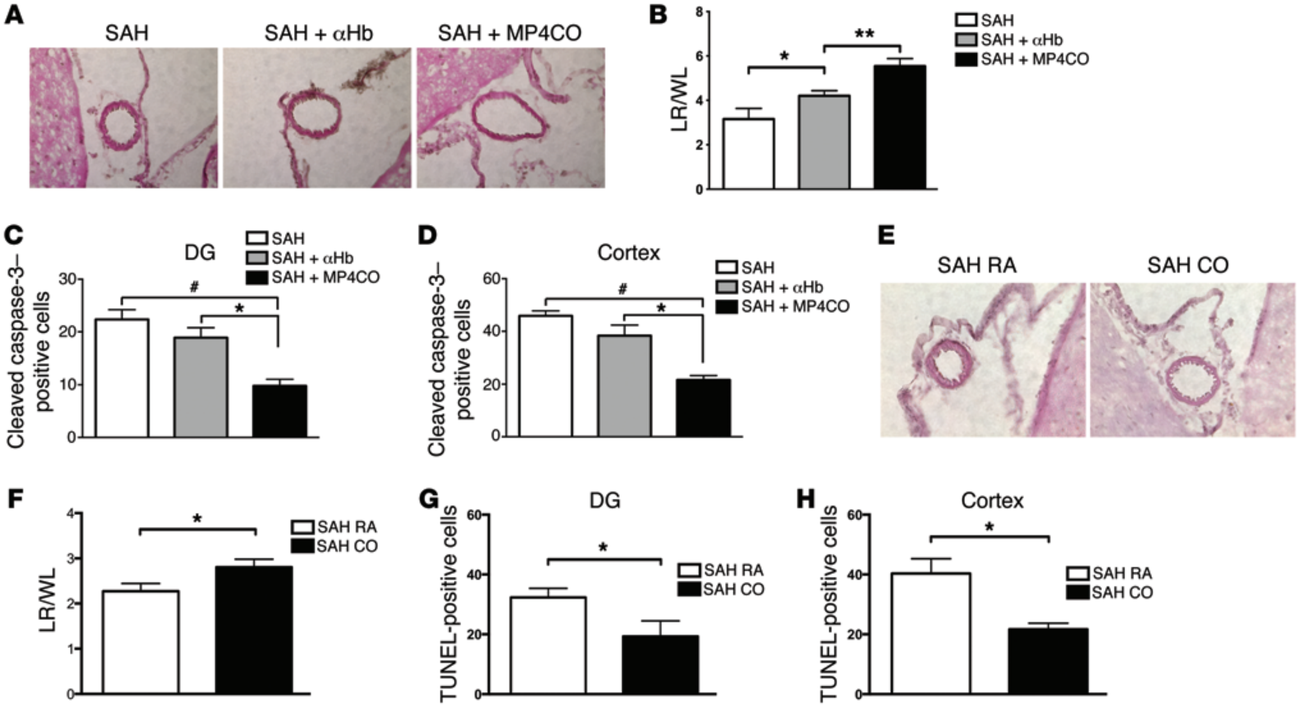

Figure 8. Alternative delivery of CO via pegylated hemoglobin and effect of CO in female mice. (**A**) Representative ($n = 6$) H&E-stained cross sections (original magnification, ×40) of the MCA after SAH in WT mice treated with CO-saturated, pegylated hemoglobin (MP4CO) or pegylated hemoglobin without CO (αHb). (**B**) Quantification of MCA vasospasm, defined as the quotient of LR and WL. $^*P = 0.0392$ for SAH versus SAH plus αHb and $^{**}P = 0.0127$ for SAH plus αHb versus SAH plus MP4CO (1-way ANOVA; $n = 6$). (**C** and **D**) Quantification of TUNEL-positive cells per microscopic field in the DG (**C**) and cortex (**D**). (**C**) $^*P = 0.0018$ for SAH plus MP4CO versus SAH plus αHb and $^\#P = 0.0003$ for SAH plus MP4CO versus SAH (1-way ANOVA; $n = 6$). (**D**) $^*P = 0.0009$ for SAH plus MP4CO versus SAH plus αHb and $^\#P = 0.0001$ for SAH plus MP4CO versus SAH (1-way ANOVA; $n = 6$). (**E**) Representative ($n = 6$) H&E-stained cross sections (original magnification, ×40) of the MCA after SAH in female WT mice treated with CO gas. (**F**) Quantification of MCA vasospasm, defined as the quotient of the LR and WL. $^*P = 0.0051$ (2-tailed Student's t test; $n = 6$). (**G** and **H**) Quantification of TUNEL-positive cells per microscopic field in the DG (**G**; $^*P = 0.0196$) and cortex (**H**; $^*P = 0.0038$) (2-tailed Student's t test; $n = 6$).

Discussion

Results obtained in this study demonstrate that microglial HO-1 expression is essential in the response to SAH by mediating clearance of blood in the subarachnoid space. Central to the beneficial effects of HO-1 are the elimination of the pro-oxidant heme burden as well as the generation of CO, which in turn regulates erythrophagocytosis. What cannot be overlooked is the added benefit of direct effects of CO on neuronal survival in vitro and in vivo due to the potent antiapoptotic effects ascribed to CO (29, 35, 36).

HO-1 induction represents an evolutionarily conserved response to cellular stress that, when activated, offers beneficial effects in numerous injury models, including the brain (8, 10). While the role of HO-1 has been well studied in the brain, most of the reports have focused on the vasoactive properties of HO-1 and less on neuroinflammation (37). Though several groups have shown that HO-1 is expressed in microglia after SAH and other forms of cerebral injury (14, 16, 17, 38–40), the exact role of HO-1 in microglia has not been defined. In this context, it is interesting to note that HO-1 likely possesses cellular functions beyond its catalytic role in heme degradation. Distinct subcellular localizations and posttranslational modifications suggest that the catalytically inactive form of HO-1 serves as a transcriptional regulator for an array of genes important in the response to oxidative stress (41–44). The fact that the noninducible isoform HO-2 is exclusively expressed in neurons and not upregulated after SAH further emphasizes the specific role of microglial HO-1 (14, 16). It also suggests that HO-derived CO reaches defined intracellular and intracompartmental concentrations that are not immediately compensated for by CO production occurring in adjacent cells. Neuronal HO-2 expression is important for neuronal resistance against excitotoxicity (45), traumatic brain injury (46), and neurotransmission (47). A role for HO-1 in neurons and astrocytes has not yet been elucidated. Using novel microglia-specific and neuron- and astrocyte-specific HO-1–KO mice, we provide evidence that, unlike microglial HO-1, neither neuronal nor astrocytic HO-1 plays a critical role in altering vasospasm, neuronal injury, or spatial memory after SAH in vivo. Neuronal and astrocytic HO-2 expression have not been studied, but our data suggest that they do not compensate for microglial HO-1 deficiency. Our results from the chimera experiments with HO-1–deficient, brain-resident microglia and HO-1–competent peripheral leukocytes (*MG-Hmox1*$^{-/-}$ *MY-Hmox1*$^{+/+}$) underscore the notion that the effects we observed are specifically due to microglial HO-1 expression or the lack thereof and not to a contribution of infiltrating peripheral leukocytes. The fact that no effect was seen when HO-1 was deleted in astrocytes and neurons further supports the specific role of microglial HO-1 in response to SAH.

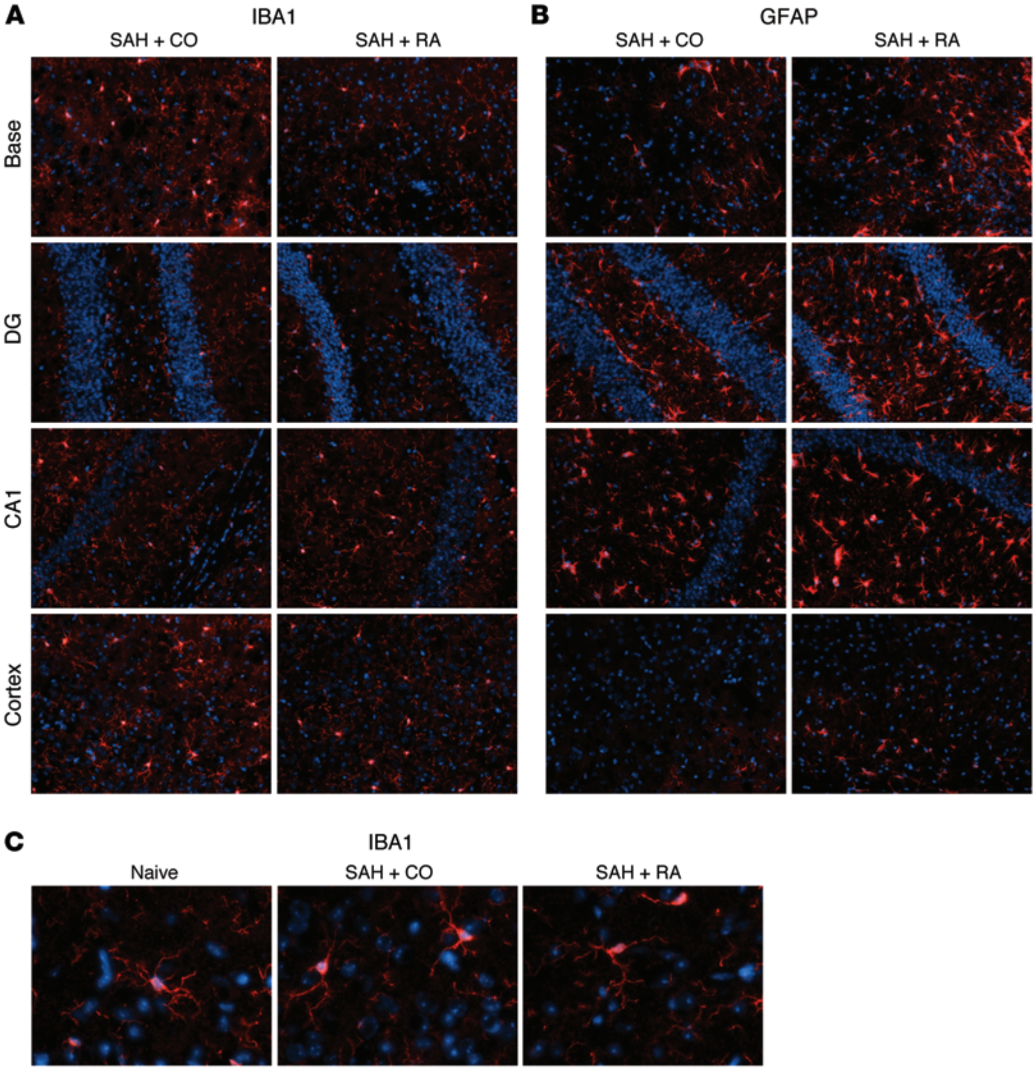

Figure 9. Gliosis in response to SAH with or without CO. (**A**) Representative images (*n* = 6) depicting IBA1 reactivity (red) in different brain regions following SAH with or without CO (original magnification, ×20; blue shows nuclear counterstaining with Hoechst 33258). (**B**) Representative images (*n* = 6) depicting IBA1 reactivity in different brain regions following SAH with or without CO (original magnification, ×20; blue shows nuclear counterstaining with Hoechst 33258). (**C**) Detailed microscopic images of IBA1-stained brain sections (*n* = 6) showing the change in microglial morphology in response to SAH, with or without CO, at the base of the brain/blood injection site (original magnification, ×40).

SAH is a type of stroke that affects approximately 40,000 people in the US each year, with an incidence of up to 10 per 100,000 per year (48, 49). Thirty to forty percent of patients will suffer long-term cognitive deficits secondary to delayed cerebral ischemia (DCI) (50). It has been a longstanding doctrine that the cognitive impairment seen after SAH is primarily attributable to vasospasm (51–53). However, recent clinical trials have failed to show beneficial effects when vasospasm was effectively ameliorated (54). These findings indicate that vasospasm is likely a marker of disease severity in SAH rather than a direct cause of DCI (55). It has become increasingly recognized that neuronal inflammation is a major contributor to DCI and subsequent neuronal impairment (56, 57).

The role of microglia in neuronal injury is a double-edged sword in that these cells can induce neuronal apoptosis via the triggering of an inflammatory response (58) but can also result in neuroprotection, which is not unlike macrophages in other tissues (59–61). The question as to which fate neurons will take in response to activated microglia most likely depends on the etiology of the injury. Here, we define a new role for microglia in response to SAH. Microglia are the principal cell type responsible for phagocytosis and elimination of rogue erythrocytes after SAH. Additionally, CO produced by microglial HO-1 is ultimately responsible for the preservation of neuronal health via increased phagocytic ability, resulting in a decreased cerebral heme burden. Controversy remains as to whether resident microglia represent a "closed" population within the brain and whether they are able to expand and migrate without recruitment and replacement from the BM (33, 62). It likely depends on the type of injury and the degree to which the BBB becomes compromised as well as on the plasticity of the microglial populations (63). Our findings show that BM-derived cells do not enter the brain unless there is significant impairment of the BBB. More important, animals subjected to SAH showed no significant mobilization of systemic leukocytes into the brain, indicating preservation of BBB integrity or lack of a chemoattractant surge. These data suggest that resident microglia remained a "closed" population that was solely responsible for the responses to the blood burden we observed.

The exact mechanisms of how the HO-1/CO axis modulates erythrophagocytosis by microglia remain to be elucidated. Red cells and the cellular components are recognized by a series of cognate receptors including CD163, CD36, and TLR4 (64–66).

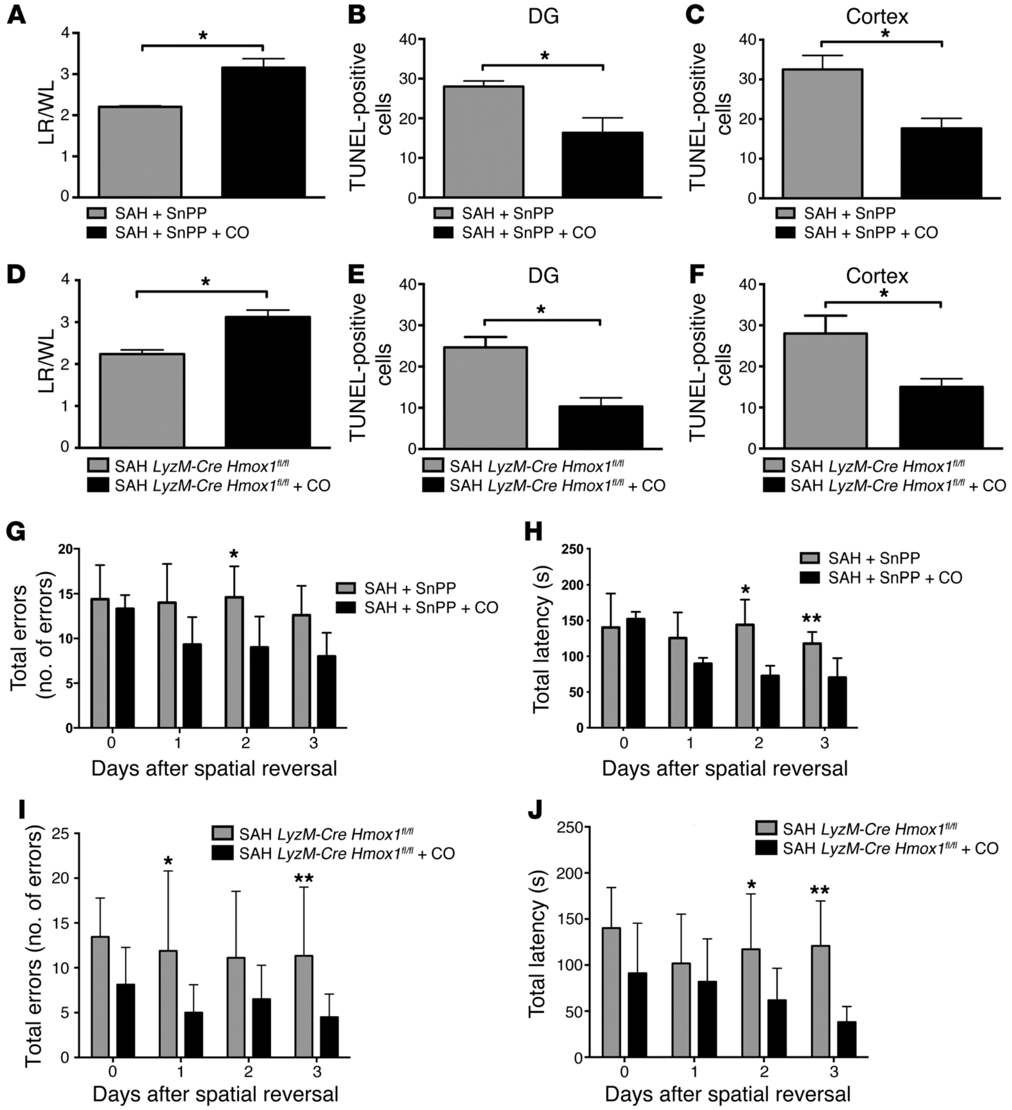

Figure 10. CO rescues increased neuronal injury due to HO-1 deficiency. (**A**) Quantification of MCA vasospasm, defined as the quotient of LR and WL. $*P = 0.0097$ for SAH plus SnPP versus SAH plus SnPP plus CO (2-tailed Student's *t* test; $n = 6$). (**B** and **C**) Quantification of TUNEL-positive cells per microscopic view in the designated brain regions. $*P = 0.0281$ for the DG (**B**) and $*P = 0.0112$ for the cortex (**C**) for SAH plus SnPP versus SAH plus SnPP plus CO (2-tailed Student's *t* test; $n = 6$). (**D**) Quantification of MCA vasospasm. $*P = 0.0014$ for SAH *LyzM-Cre Hmox1*$^{fl/fl}$ versus SAH *LyzM-Cre Hmox1*$^{fl/fl}$ plus CO (2-tailed Student's *t* test; $n = 6$). (**E** and **F**) Quantification of TUNEL-positive cells per microscopic view in the DG (**E**; $*P = 0.0016$) and cortex (**F**; $*P = 0.0093$) for SAH *LyzM-Cre Hmox1*$^{fl/fl}$ versus SAH *LyzM-Cre Hmox1*$^{fl/fl}$ plus CO (2-tailed Student's *t* test; $n = 6$). (**G**) Number of total errors in spatial memory function by Barnes maze assessment. $*P = 0.0301$ (day 2) for SAH plus SnPP versus SAH plus SnPP plus CO (2-way ANOVA; $n = 9$). (**H**) Total latency in seconds for spatial memory function by Barnes maze assessment. $*P = 0.0006$ (day 2) and $**P = 0.0301$ (day 3) for SAH plus SnPP versus SAH plus SnPP plus CO (2-way ANOVA; $n = 9$). (**I**) Number of total errors in spatial memory function by Barnes maze assessment. $*P = 0.0231$ (day 1) and $**P = 0.0246$ (day 3) for SAH *LyzM-Cre Hmox1*$^{fl/fl}$ versus SAH *LyzM-Cre Hmox1*$^{fl/fl}$ plus CO (2-way ANOVA; $n = 9$). (**J**) Total latency in seconds for spatial memory function by Barnes maze assessment. $*P = 0.0233$ and $**P = 0.0003$ for SAH *LyzM-Cre Hmox1*$^{fl/fl}$ versus SAH *LyzM-Cre Hmox1*$^{fl/fl}$ plus CO (2-way ANOVA; $n = 9$).

Whether one or more of these receptors is involved in phagocytosis and blood clearance has not been evaluated. It is also important to note that it remains an unsolved question whether exogenous delivery of CO equals the distinct intracompartmental and subcellular concentrations of CO produced endogenously via HO and whether exogenous CO can fully substitute for the lack of endogenous production. However, endogenous and exogenous CO provided comparable protection in our SAH model, and others (67) have shown that endogenous and exogenous CO has similar effects on mitochondrial respiration.

Importantly, our findings are translated to and corroborated in patients in whom we observed that SAH signals to the periphery, resulting in elevated HO-1 in peripheral leukocytes. This could also be unrelated to brain injury and reflect peripheral events related to the patient's status. HO-1 has been shown to be important in the recruitment and migration of BM progenitors in other organs (68). Whether peripheral HO-1 is involved in the response to injury in the brain, or reflects a more general systemic stress response, remains to be determined. While our clinical data support a potential role for HO-1 in human SAH, as evidenced by a significant

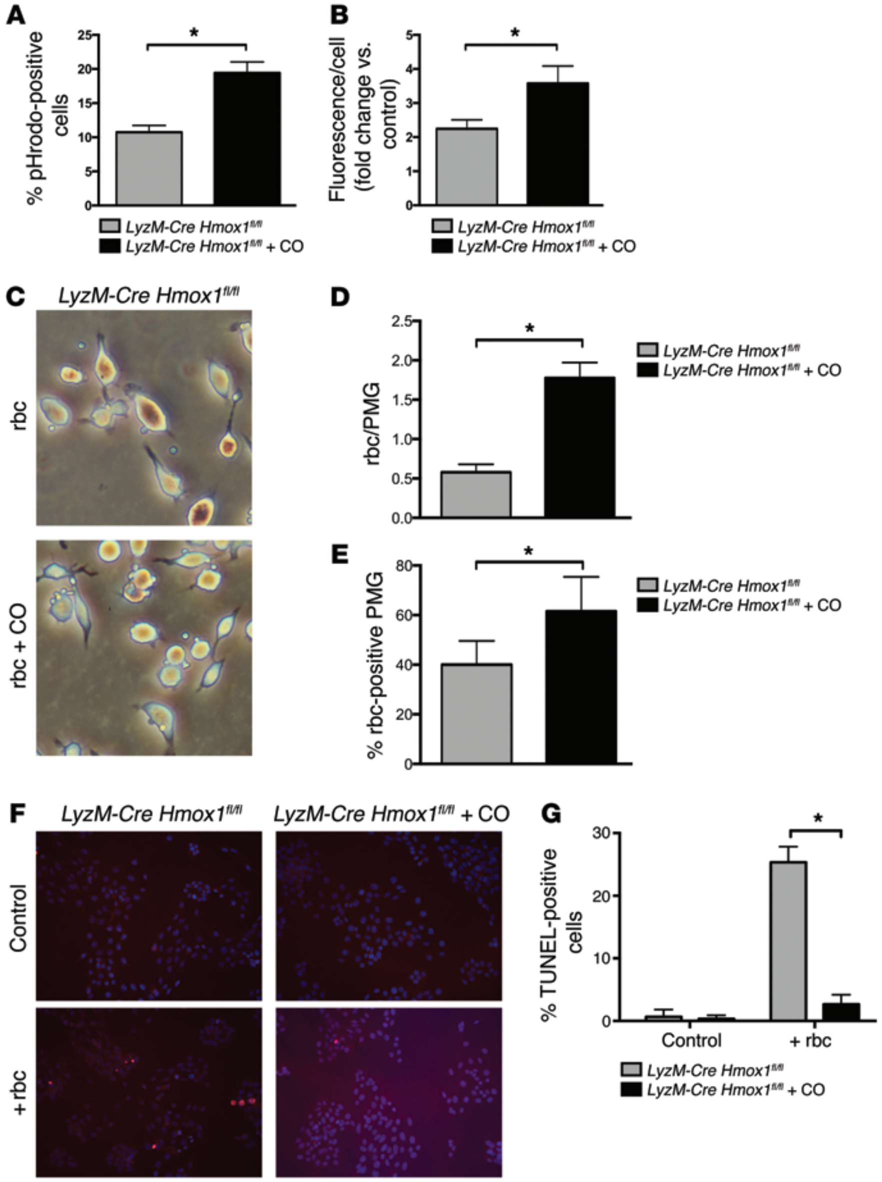

Figure 11. CO rescues HO-1 deficiency and impaired erythrophagocytosis, leading to increased cell death in vitro. (**A**) Quantification of the percentage of microglia positive for fluorescence-labeled red blood cells by flow cytometric analysis. *$P = 0.0013$ for *LyzM-Cre Hmox1*$^{fl/fl}$ red blood cells versus *LyzM-Cre Hmox1*$^{fl/fl}$ red blood cells plus CO (2-tailed Student's t test; $n = 3$). (**B**) Mean fluorescent signal in microglial cells after exposure to fluorescence-labeled red blood cells. *$P = 0.0154$ for *LyzM-Cre Hmox1*$^{fl/fl}$ red blood cells versus *LyzM-Cre Hmox1*$^{fl/fl}$ red blood cells plus CO (2-tailed Student's t test; $n = 3$). (**C**) Representative light microscopic images (original magnification, ×40; $n = 3$) of *LyzM-Cre Hmox1*$^{fl/fl}$ microglia after exposure to red blood cells with or without CO. (**D**) Quantification of red blood cells per microglia, analyzed by light microscopy. *$P < 0.0001$ for *LyzM-Cre Hmox1*$^{fl/fl}$ red blood cells versus *LyzM-Cre Hmox1*$^{fl/fl}$ red blood cells plus CO (2-tailed Student's t test; $n = 3$). (**E**) Quantification of the percentage of red blood cell–positive microglia by light microscopy. *$P = 0.0107$ for *LyzM-Cre Hmox1*$^{fl/fl}$ red blood cells versus *LyzM-Cre Hmox1*$^{fl/fl}$ red blood cells plus CO (2-tailed Student's t test; $n = 3$). (**F**) Representative images (original magnification, ×20; $n = 3$) of TUNEL staining (red) of neuronal cells cocultured with *LyzM-Cre Hmox1*$^{fl/fl}$ microglia with or without red blood cells and CO. Cell nuclei were counterstained with Hoechst 33258 (blue). (**G**) Quantification of TUNEL-positive neuronal cells per microscopic view. *$P < 0.0001$ for *LyzM-Cre Hmox1*$^{fl/fl}$ red blood cells versus *LyzM-Cre Hmox1*$^{fl/fl}$ red blood cells plus CO (2-tailed Student's t test; $n = 3$).

correlation between HO-1 expression, inflammatory milieu, and CHV, our data do not allow us to draw any conclusion regarding HO-1 and clinical outcome after SAH because of the small sample size. Moreover, we must consider that the elevated bilirubin levels detected in the CSF reflect total HO activity (*Hmox1* and *Hmox2*) and may involve other cell types in the brain where heme catabolism is occurring, leading to bilirubin accumulation in the CSF. However, given the potent effects of CO in our mouse model of SAH, further clinical investigation is warranted. In the future, inhaled CO might be a potential treatment for patients diagnosed with this devastating form of hemorrhagic stroke.

Methods

Animals and anesthesia. Male or female C57BL/6 mice were obtained from The Jackson Laboratory (stock 000664). Cell-specific HO-1 KO in microglia (*LyzM-Cre Hmox1*$^{fl/fl}$) was achieved by crossing *Hmox1*$^{fl/fl}$ mice (stock RBRC03163; RIKEN BioResource Center) with mice expressing Cre recombinase under the lysozyme (*LyzM*) promoter (stock 004781; The Jackson Laboratory). Cell-specific HO-1 KO in astrocytes and neurons (*Nes-Cre Hmox1*$^{fl/fl}$) was achieved by crossing *Hmox1*$^{fl/fl}$ mice with mice expressing Cre recombinase under the nestin (*Nes*) promoter (stock 003771; The Jackson Laboratory). *Hmox1*$^{fl/fl}$ mice served as the controls for experiments involving *LyzM-Cre Hmox1*$^{fl/fl}$ and *Nes-Cre Hmox1*$^{fl/fl}$ mice. *CX3cr1-GFP* mice (B6.129P-*Cx3cr1*^{tm1Litt}/J, stock 005582) and WT animals with a CD45.1 allele (B6.SJL-*Ptprc*^{a} *Pepc*^{b}/BoyJ, stock 002104) were purchased from The Jackson Laboratory. Animals were fed a standard rodent diet ad libitum while kept on a 12-hour light/12-hour dark cycle. All surgical procedures and manipulations were performed under general anesthesia with ketamine (10 mg/kg) and xylazine (4 mg/kg) and body temperature maintenance. At surgery, buprenorphine (50 μg/kg) was applied s.c. to treat possible pain.

SAH stroke model. SAH in 10- to 12-week-old mice was achieved by prechiasmatic injection of autologous blood. In brief, after induction of anesthesia, the head was fixed in a stereotactic apparatus. With a midline incision, the skin overlying the anterior skull was opened. A burr hole was drilled into the skull 4.5 mm anterior to the bregma with a caudal angel of 40° using a 0.9-mm drill. Blood (60 μl) was withdrawn from a C57BL/6 WT blood donor and injected over a 10-second period with a 27-gauge needle advanced through the burr hole at a 40° angle until reaching the base of the skull. The needle was left in place for 5 minutes to avoid backflow.

SnPP IX, CO gas, and MP4CO/αHb treatment. After SAH, animals were randomly assigned to receive treatment with either CO or synthetic air for 1 hour. CO exposure was administered in a custom-made gas exposure chamber. Animals had free access to food and water during the exposure. CO gas (1%) was mixed with synthetic air to achieve 250 ppm. CO concentration was monitored continuously throughout the application by an infrared gas analyzer. Treatment was started immediately after the SAH procedure and repeated every 24 hours for 7 days. For HO inhibition, animals were injected s.c. with 40 μM/kg SnPP IX (Frontier Scientific) daily during the Barnes maze training period (see below) and after SAH for 7 days. CO-saturated, pegylated hemoglobin (MP4CO, 12 ml/kg) or pegylated hemoglobin without CO (αHb, 12 ml/kg) (both supplied by Sangart Inc.) was given via daily penile injection for 7 days immediately following SAH.

Barnes maze for spatial learning evaluation. Cognitive function and spatial learning was tested on the Barnes maze as described previously, with minor modification. In brief, the paradigm consisted of a white circular platform with a diameter of 90 cm. Along the perimeter of the platform, 20 equal-sized holes were located. One hole led to a box to which the animals could escape from the open platform. As an aversive stimulus, a bright light source was placed above the platform. We introduced an additional reward stimulus by placing food in the escape box. Cardboard placards with different visual cues were placed around the platform. The location of the escape box and the visual cues were kept constant during the initial acquisition period. Prior to SAH, the mice underwent spatial acquisition for 7 days, with 3 trials per animal per day. Animals were allowed to explore the maze for 3 minutes. Once they entered the escape box, they were allowed to remain in the box for 1 minute. The inter-trial interval was 15 minutes for each animal, with extensive cleaning of the platform after each animal to eliminate olfactory cues. Animals that did not enter the escape box within 3 minutes were guided to the correct hole. Surrogates for cognitive function were measured: specifically, the total time required for the mouse to find the goal box (latency) and the number of holes the animal explored before finding the goal box (error number). After 7 days of acquisition, SAH was performed as described above. Spatial memory testing, which consisted of 1 trial per animal per day, was started on day 1 after SAH and continued for 7 days. To test for flexibility and relearning, the location of the goal box was moved 180° from its original position on day 4 (spatial reversal), while visual cues were kept at the initial position. Maze procedures were performed by an investigator blinded to the genotype and treatment groups.

Morris water maze test for spatial learning evaluation. As a second test for spatial learning performance, we used the Morris water maze test as described previously, with minor modification. In brief, a white circular tank with a diameter of 120 cm and a height of 50 cm was filled with opaque water. A circular platform with a diameter of 12 cm was submerged 1 cm below the water's surface and placed in a specific quadrant of the maze. Around the maze, we placed cardboard placards depicting different objects as distant visual cues. The location of the platform and the visual cues were kept constant during the acquisition phase. Prior to SAH, spatial acquisition was performed for 7 days, with 3 trials per animal per day. Each animal was started from 3 different locations each day, represented by the 3 quadrants of the maze where the platform was not placed. The order of the starting positions was rotated daily. The time limit per trial was set to 1 minute, and the inter-trial interval was 5 minutes for each animal. Once the animal reached the platform, it was allowed to sit on the platform for 15 seconds. Animals that did not reach the platform within 1 minute were guided toward it. As a surrogate for cognitive function, the total time required for the mouse to find the platform (latency) was measured. After 7 days of acquisition, SAH and CO treatments were administered as described above. Spatial memory testing, which consisted of 1 trial per animal per day, was started on day 1 after SAH and continued for 7 days. To test for the ability to extinguish the initial learning and acquire memory for a new platform position, the location of the platform was moved to the quadrant on the opposite side of the maze on day 4 (spatial reversal), while visual cues were kept at the initial position. An investigator blinded to treatment groups performed the maze procedures.

H&E staining and evaluation of cerebral vasospasm. Seven days after SAH, animals were deeply anesthetized with ketamine and xylazine and transcardially perfused with TBS using a peristaltic pump at a flow rate of 3 ml/minute. Brains were removed and postfixed in 4% PFA for 18 hours. After cryoprotection in sucrose, brains were frozen, cut in 9-μm sections, and stained with H&E. Representative digital images of 3 consecutive middle cerebral artery (MCA) cross sections from each animal were obtained, and the lumen radius/wall thickness ratio was quantified to assess vasospasm using ImageJ software (NIH).

IHC and TUNEL staining. Frozen brains were cut in 9-μm serial coronal sections. Sections were post-fixed with 2% PFA for 10 minutes and permeabilized with 0.5% Triton X-100/PBS for 10 minutes. Slides were then blocked in horse serum (7% in PBS) for 30 minutes at room temperature. Staining was performed with primary antibodies against cleaved caspase-3 (1:100; catalog 9664; Cell Signaling Technology) and NeuN (1:200; catalog MAB377; EMD Millipore) at 4°C overnight. Sections were then conjugated with their corresponding secondary antibody for fluorescence (1:600 Alexa Fluor 488 donkey anti-mouse and 1:300 Alexa Fluor 594 donkey anti-rabbit; Invitrogen). Nuclear counterstaining was done with Hoechst 33258 (1:10,000; 3 min; Sigma-Aldrich), and slides were examined under a fluorescence microscope. To achieve appropriate consistency in cell quantification, 3 images were obtained for each area of interest to quantify positive cells. Quantification was performed in a standardized fashion. Tissue sections were obtained 1.5–1.9 mm dorsal from the bregma as determined by a stereotactic mouse atlas. The subregions of the anterior hippocampus (cornu ammonis and DG) and adjacent cortex were analyzed for neuronal apoptosis.

For TUNEL staining, slides were fixed in 4% PFA for 20 minutes and permeabilized with 0.1% Triton X-100 for 2 minutes. After washing with PBS, sections were covered with enzyme and label solution (In Situ Cell Death Detection Kit, TMR Red; Roche Life Science) for 1 hour at 37°C in a humidified atmosphere. Nuclear counterstaining and quantification were performed as described above.

PMG cell culture and treatment. PMG were isolated from mice at P5 to P7 by enzymatic neural dissociation (Papain Neural Dissociation Kit; Miltenyi Biotec) and in vitro mixed glia culture. In brief, mouse brains were enzymatically dissociated according to the manufacturer's instructions, and the resulting mixed glia culture containing astrocytes and microglia was cultivated in DMEM containing penicillin-streptomycin, 10% FBS, and M-CSF (10 ng/ml) in a humidified atmosphere with 5% CO_2. After 1 week of cultivation, cell culture plates were shaken at 200 rpm for 2 hours every 2 to 3 days. Floating microglia were collected from the supernatant and seeded onto 6-well plates for experiments at a density of 2×10^5 cells per well. Microglial phenotype was confirmed by CD11b staining and flow cytometry (see below) for every experiment.

For erythrophagocytosis experiments, 100 μl blood was drawn from the mandibular vein of a C57BL/6 WT animal, washed with PBS, and stained with 35 μM amine-reactive, pH-sensitive fluorescent ester dye (pHrodo Green STP Ester; Life Technologies) in 1 ml PBS for 30 minutes. PMG were incubated with 100 μl labeled red blood cell suspension for 1 hour before use. In selected experiments, phagocytosis was blocked with cytochalasin D (10 μM, 30-min pretreatment; Sigma-Aldrich) or dynasore (50 μM, 30-min pretreatment; Sigma-Aldrich). Cells in which we wanted to study the role of CO were transferred to an air-tight, humidified chamber (C-Chamber; Biospherix) after starting the red blood cell exposure and exposed to 250 ppm CO and 5% CO_2 for 1 hour, which was controlled by an automated gas delivery system (Oxycycler C42; Biospherix).

Light microscopy. After red blood cell exposure, cells were washed with PBS 3 times to remove any remaining unphagocytized red blood cells. For each well, 3 representative images (original magnification, ×10) were taken using an inverted light microscope with a camera port (Telaval 31; Zeiss). For every image, the number of red blood cells per PMG and the percentage of red blood cell–positive PMG were determined using ImageJ software.

Flow cytometry. After light microscopic analysis, cells were harvested with a cell lifter, washed with flow cytometric buffer (PBS with 1% BSA, 2 mM EDTA, and 0.05% Na-azide), and stained with a PE-Cy7–tagged CD11b antibody (1:100, 30 min; BioLegend). Flow cytometry was performed on a FACSCalibur (BD Biosciences), with selection of CD11b-positive PMG and detection of phagocytosis-related fluorescence in FL-1. The relative percentage of red blood cell–positive PMG and the mean fluorescence per PMG were calculated using FlowJo software.

Western blot analysis. Cells were washed with PBS and lysed in radioimmunoprecipitation assay (RIPA) buffer with 1 freeze/thaw cycle and sonification. Equal amounts of protein were separated on a 10% SDS polyacrylamide gel and transferred to a nitrocellulose membrane. Membranes were blocked with 5% skim milk in Tween-20/TBS and incubated in the recommended dilution of specific antibodies (HO-1; 1:1,000; Abcam) overnight at 4°C. Membranes were then incubated with the corresponding secondary antibody for infrared fluorescence detection and developed on an Odyssey infrared imaging system (LI-COR).

Coculture experiments. Murine hippocampal HT22 cells (gift of Joseph Burdo, Biology Department, Boston College, Boston, Massachusetts, USA) were grown in DMEM containing penicillin-streptomycin and 10% FBS. For coculture experiments, cells were plated on 24-mm coverslips (Neuvitro) at a density of 3×10^5. Coverslips were placed into 6-well plates. PMG were plated on 18-mm coverslips (Neuvitro), inserted into 3-μM Transwell chambers (EMD Millipore) at a density of 1×10^5, and placed onto the HT22 wells immediately before the start of the experiment. Blood, with or without inhibitors, was added to the PMG-containing upper chamber of the coculture, set up at concentrations of 10 μM cytochalasin and 50 μM dynasore. TUNEL staining of the HT22 was done as described above. Quantification of TUNEL-positive cells was performed by capturing 3 representative images per coverslip and calculating the percentage of TUNEL-positive cells to account for differences in cell density. PMG were stained with antibodies against IBA1 and TER119 to assess phagocytosis by fluorescence microscopy.

In vivo hemorrhage imaging. For hemorrhage imaging, blood labeled with gadopentetate dimeglumine was injected into the subarachnoid space as described above. Animals were then treated with CO (250 ppm) or RA for 1 hour (WT experiment only), and T1-weighted images were acquired on a 9.4 Tesla MRI 8 hours after SAH ($n = 3$ per group). The hematoma volume was calculated using OsiriX software as follows: the hematoma area in 3 adjacent sagittal slices (0.5 mm slice thickness) in both directions from the midline sagittal (6 slices total per animal) was measured and the volume calculated using the measured areas and the known slice thickness.

Human sample collection and analysis. CSF and blood samples were acquired from consecutive SAH patients admitted to the neuro-ICU on days 1 and 7 and from patients with unruptured cerebral aneurysms (controls). RNA from CSF cells was isolated with TRIzol, concentrated by spin-column purification (RNeasy Micro Kit; QIAGEN), and cDNA libraries were acquired by reverse transcription (iScript cDNA Synthesis Kit; Bio-Rad). Gene expression of HO-1 was analyzed by real-time PCR (SYBR Green Master Mix; Agilent Technologies), with *Rpl13a* used as a reference gene.

Primer sequences were as follows: HO-1, forward: GTGATAGAAGAGGCCAAGACTG, reverse: GAATCTTGCACTTTGTTGCTGG; and *Rpl13a*, forward: CGCTGTGAAGGCATCAACATTTC, reverse: GCTGTCACTGCCTGGTACTTC.

Bilirubin, hemoglobin, and protein content in the CSF was analyzed by spectrometry as described previously (69). In brief, absorbance at 340, 415, and 460 nm was measured, and bilirubin (c1), hemoglobin (c2), and protein (c3) content was calculated using the following formulas:

(a) $A_{340} = 0.012 * c1 + 0.0015 * c2 + 0.000054 * c3$

(b) $A_{415} = 0.049 * c1 + 0.0069 * c2 + 0.000016 * c3$

(c) $A_{460} = 0.083 * c1 + 0.0006 * c2 + 0.000007 * c3$

Blood samples were drawn into RNA-stabilizing tubes (Tempus Blood RNA Tubes; Applied Biosystems), and peripheral blood RNA was isolated using spin-column purification (Tempus Spin RNA Isolation Kit; Applied Biosystems). Gene expression was analyzed as described above.

HO-1 expression and bilirubin content in SAH patients were compared with radiographic subarachnoid hematoma volume in the cisterns surrounding the pons and the midbrain (CHV, calculated using OsiriX software). CHV was calculated as follows: cisternal hematoma (specifically, the prepontine cistern, the interpeduncular cistern, and the ambient cisterns) areas at the level of the caudal pons extending superiorly to the midbrain in 4 adjacent axial CT slices (5 mm slice thickness) were measured, and hematoma volumes were calculated using the measured areas and the known slice thickness.

Whole-body irradiation with head protection and BM transplantation. For establishment and validation of the BM transplant (BMTx) model, we first performed whole-body irradiation (12 Gy) in WT mice, followed by infusion via the penile vein of BM cells (5×10^6 cells/

animal) from *Cx3cr1-GFP* mice (B6.129P-*Cx3cr1*^{tm1Litt}/J, The Jackson Laboratory) on the same day. *Cx3cr1-GFP* mice showed GFP expression in all cells expressing Cx3cr1, including most cells emerging from the granulocyte-macrophage cell lineage such as macrophages, monocytes, microglia, and neutrophils, but also NK cells, DCs, and cells of the lymphoid lineage (70–75). In 1 group of animals, the head was shielded from radiation with a combined outer lead block (2 cm thickness) and inner lead helmet (0.17 cm thickness to shield from scattered radiation). One week after transplantation, peripheral blood leukocytes were isolated and analyzed for GFP positivity by cytospinning and fluorescence microscopy. A period of 4 weeks was allowed for full consolidation of the transplanted BM. GFP positivity of the BM was confirmed by flow cytometry at this time point. In addition, engraftment of GFP-positive cells into peripheral organs (spleen, liver, lung) and the brain, with or without head shielding, was determined by fluorescence microscopy. In a separate cohort of animals, SAH was induced 4 weeks after transplantation, as described above, to study the effect of SAH on the invasion of BM-derived cells into the brain, with or without head shielding. Cell invasion into the brain was determined 1 week after SAH by fluorescence microscopy.

In a second set of experiments, we transplanted 5 × 10^6 BM cells per animal from HO-1–expressing WT animals (B6.SJL-*Ptprc*^{a} *Pepc*^{b}/BoyJ, The Jackson Laboratory; this congenic C57BL/6 mouse carries the differential CD45.1 allele that allows for transplant detection) into *LyzM-Cre Hmox1*$^{fl/fl}$ (*MG-Hmox1*$^{-/-}$ *MY-Hmox1*$^{+/+}$) and *Hmox1*$^{fl/fl}$ (*MG-Hmox1*$^{+/+}$ *MY-Hmox1*$^{+/+}$) mice with head shielding. We allowed 4 weeks for complete BM consolidation before SAH was induced as described above. Analysis of vasospasm, neuronal cell death, and spatial memory function was performed as described above.

Statistics. Data were analyzed using GraphPad Prism, version 6 (GraphPad Software). Results are presented as the mean ± SD. Two groups were compared with a 2-tailed Student's *t* test, while multiple groups were compared using 1-way ANOVA with Bonferroni's post-hoc test. Data from spatial memory function testing (Barnes maze, water maze) with repetitive measurements on individual animals were analyzed using repeated-measures 2-way ANOVA with Bonferroni's post-hoc test (factor A: time, factor B: genotype or treatment, respectively). Correlation was described using Spearman's correlation coefficient. A *P* value of less than 0.05 was considered statistically significant. In vivo sample sizes were 6 per group, except for behavior experiments ($n = 9$) and MRI ($n = 3$). In vitro experiments were repeated 3 times. All allocations of animals to experimental groups were randomized, as were the in vitro studies. Analysis of TUNEL cell counts, vasospasm, in vitro phagocytosis, and hematoma volume was done in a blinded manner.

Study approval. All procedures involving animals were approved by the IACUC and the Radiation Safety Office (RSO) of Beth Israel Deaconess Medical Center. Patients participated in this study under a protocol for acquiring CSF and blood samples that was approved by the IRB of Beth Israel Deaconess Medical Center and provided written informed consent.

Acknowledgments

This work was largely supported by grants from the NIH (K08 NS078048, to K.A. Hanafy, and HL-071797 and HL-076167, to L.E. Otterbein) and the German Research Foundation (DFG) (SCHA 1838/2-1, to N. Schallner). We thank Jonathan S. Jozokos for his assistance with the irradiation experiment and the Julie Henry Fund at the Transplant Center of the Beth Israel Deaconess Medical Center for their support.

Address correspondence to: Khalid A. Hanafy, Assistant Professor of Neurology, Harvard Medical School, Division of Neurointensive Care Medicine, Beth Israel Deaconess Medical Center, 3 Blackfan Circle, Boston, Massachusetts 02140, USA. Phone: 617.735.2836; E-mail: khanafy@bidmc.harvard.edu.

1. Otterbein LE, Kolls JK, Mantell LL, Cook JL, Alam J, Choi AM. Exogenous administration of heme oxygenase-1 by gene transfer provides protection against hyperoxia-induced lung injury. *J Clin Invest*. 1999;103(7):1047–1054.
2. Zuckerbraun BS, et al. Carbon monoxide protects against liver failure through nitric oxide-induced heme oxygenase 1. *J Exp Med*. 2003;198(11):1707–1716.
3. Tayem Y, Green CJ, Motterlini R, Foresti R. Isothiocyanate-cysteine conjugates protect renal tissue against cisplatin-induced apoptosis via induction of heme oxygenase-1. *Pharmacol Res*. 2014;81:1–9.
4. Clark JE, Foresti R, Sarathchandra P, Kaur H, Green CJ, Motterlini R. Heme oxygenase-1-derived bilirubin ameliorates postischemic myocardial dysfunction. *Am J Physiol Heart Circ Physiol*. 2000;278(2):H643–H651.
5. Wegiel B, Nemeth Z, Correa-Costa M, Bulmer AC, Otterbein LE. Heme oxygenase-1: a metabolic nike. *Antioxid Redox Signal*. 2014;20(11):1709–1722.
6. Sun MH, et al. Retinal protection from acute glaucoma-induced ischemia-reperfusion injury through pharmacologic induction of heme oxygenase-1. *Invest Ophthalmol Vis Sci*. 2010;51(9):4798–4808.
7. Shimada Y, Tsunoda H, Zang L, Hirano M, Oka T, Tanaka T. Synergistic induction of heme oxygenase-1 by nicaraven after subarachnoid hemorrhage to prevent delayed cerebral vasospasm. *Eur J Pharmacol*. 2009;620(1–3):16–20.
8. Zhang F, et al. Pharmacological induction of heme oxygenase-1 by a triterpenoid protects neurons against ischemic injury. *Stroke*. 2012;43(5):1390–1397.
9. Saleem S, Zhuang H, Biswal S, Christen Y, Dore S. Ginkgo biloba extract neuroprotective action is dependent on heme oxygenase 1 in ischemic reperfusion brain injury. *Stroke*. 2008;39(12):3389–3396.
10. Wang HQ, Xu YX, Zhu CQ. Upregulation of heme oxygenase-1 by acteoside through ERK PI3 K/Akt pathway confer neuroprotection against beta-amyloid-induced neurotoxicity. *Neurotox Res*. 2012;21(4):368–378.
11. Chen G, Fang Q, Zhang J, Zhou D, Wang Z. Role of the Nrf2-ARE pathway in early brain injury after experimental subarachnoid hemorrhage. *J Neurosci Res*. 2011;89(4):515–523.
12. Foresti R, et al. Small molecule activators of the Nrf2-HO-1 antioxidant axis modulate heme metabolism inflammation in BV2 microglia cells. *Pharmacol Res*. 2013;76:132–148.
13. Sutherland BA, Rahman RM, Clarkson AN, Shaw OM, Nair SM, Appleton I. Cerebral heme oxygenase 1 and 2 spatial distribution is modulated following injury from hypoxia-ischemia middle cerebral artery occlusion in rats. *Neurosci Res*. 2009;65(4):326–334.
14. Matz P, Turner C, Weinstein PR, Massa SM, Panter SS, Sharp FR. Heme-oxygenase-1 induction in glia throughout rat brain following experimental subarachnoid hemorrhage. *Brain Res*. 1996;713(1–2):211–222.
15. Takeda A, Kimpara T, Onodera H, Itoyama Y, Shibahara S, Kogure K. Regional difference in induction of heme oxygenase-1 protein following rat transient forebrain ischemia. *Neurosci Lett*. 1996;205(3):169–172.
16. Turner CP, Panter SS, Sharp FR. Anti-oxidants prevent focal rat brain injury as assessed by induction of heat shock proteins (HSP70, HO-1/HSP32, HSP47) following subarachnoid injections of lysed blood. *Brain Res Mol Brain Res*. 1999;65(1):87–102.
17. Matz PG, Weinstein PR, Sharp FR. Heme oxygenase-1 and heat shock protein 70 induction in

glia neurons throughout rat brain after experimental intracerebral hemorrhage. *Neurosurgery*. 1997;40(1):152–160.

18. Fukuda K, Panter SS, Sharp FR, Noble LJ. Induction of heme oxygenase-1 (HO-1) after traumatic brain injury in the rat. *Neurosci Lett*. 1995;199(2):127–130.
19. Kuroki M, Kanamaru K, Suzuki H, Waga S, Semba R. Effect of vasospasm on heme oxygenases in a rat model of subarachnoid hemorrhage. *Stroke*. 1998;29(3):683–688.
20. Otterbein LE, Mantell LL, Choi AM. Carbon monoxide provides protection against hyperoxic lung injury. *Am J Physiol*. 1999;276(4 pt 1):L688–L694.
21. Otterbein LE, et al. Carbon monoxide has anti-inflammatory effects involving the mitogen-activated protein kinase pathway. *Nat Med*. 2000;6(4):422–428.
22. Song R, et al. Carbon monoxide induces cytoprotection in rat orthotopic lung transplantation via anti-inflammatory and anti-apoptotic effects. *Am J Pathol*. 2003;163(1):231–242.
23. Zhang X, Shan P, Alam J, Davis RJ, Flavell RA, Lee PJ. Carbon monoxide modulates Fas/Fas ligand, caspases, and Bcl-2 family proteins via the p38alpha mitogen-activated protein kinase pathway during ischemia-reperfusion lung injury. *J Biol Chem*. 2003;278(24):22061–22070.
24. Wu L, Wang R. Carbon monoxide: endogenous production, physiological functions, and pharmacological applications. *Pharmacol Rev*. 2005;57(4):585–630.
25. Ryter SW, Alam J, Choi AM. Heme oxygenase-1/carbon monoxide: from basic science to therapeutic applications. *Physiol Rev*. 2006;86(2):583–650.
26. Goebel U, et al. Carbon monoxide inhalation reduces pulmonary inflammatory response during cardiopulmonary bypass in pigs. *Anesthesiology*. 2008;108(6):1025–1036.
27. Yabluchanskiy A, Sawle P, Homer-Vanniasinkam S, Green CJ, Foresti R, Motterlini R. CORM-3, a carbon monoxide-releasing molecule, alters the inflammatory response reduces brain damage in a rat model of hemorrhagic stroke. *Crit Care Med*. 2012;40(2):544–552.
28. Motterlini R, Otterbein LE. The therapeutic potential of carbon monoxide. *Nat Rev Drug Discov*. 2010;9(9):728–743.
29. Vieira HL, Queiroga CS, Alves PM. Pre-conditioning induced by carbon monoxide provides neuronal protection against apoptosis. *J Neurochem*. 2008;107(2):375–384.
30. Almeida AS, Queiroga CS, Sousa MF, Alves PM, Vieira HL. Carbon monoxide modulates apoptosis by reinforcing oxidative metabolism in astrocytes: role of Bcl-2. *J Biol Chem*. 2012;287(14):10761–10770.
31. Zeynalov E, Dore S. Low doses of carbon monoxide protect against experimental focal brain ischemia. *Neurotox Res*. 2009;15(2):133–137.
32. Biermann J, Lagreze WA, Dimitriu C, Stoykow C, Goebel U. Preconditioning with inhalative carbon monoxide protects rat retinal ganglion cells from ischemia/reperfusion injury. *Invest Ophthalmol Vis Sci*. 2010;51(7):3784–3791.
33. Mildner A, et al. Microglia in the adult brain arise from Ly-6ChiCCR2^{+} monocytes only under defined host conditions. *Nat Neurosci*. 2007;10(12):1544–1553.
34. Roof RL, Hall ED. Gender differences in acute CNS trauma and stroke: neuroprotective effects of estrogen and progesterone. *J Neurotrauma*. 2000;17(5):367–388.
35. Brouard S, et al. Carbon monoxide generated by heme oxygenase 1 suppresses endothelial cell apoptosis. *J Exp Med*. 2000;192(7):1015–1026.
36. Dallas ML, et al. Carbon monoxide protects against oxidant-induced apoptosis via inhibition of Kv2.1. *FASEB J*. 2011;25(5):1519–1530.
37. Ogawa T, et al. Protein therapy using heme-oxygenase-1 fused to a polyarginine transduction domain attenuates cerebral vasospasm after experimental subarachnoid hemorrhage. *J Cereb Blood Flow Metab*. 2011;31(11):2231–2242.
38. Liu Y, Zhang Z, Luo B, Schluesener HJ, Zhang Z. Lesional accumulation of heme oxygenase-1^{+} microglia/macrophages in rat traumatic brain injury. *Neuroreport*. 2013;24(6):281–286.
39. Parada E, et al. The microglial alpha7-acetylcholine nicotinic receptor is a key element in promoting neuroprotection by inducing heme oxygenase-1 via nuclear factor erythroid-2-related factor 2. *Antioxid Redox Signal*. 2013;19(11):1135–1148.
40. Nakaso K, et al. Co-induction of heme oxygenase-1 and peroxiredoxin I in astrocytes microglia around hemorrhagic region in the rat brain. *Neurosci Lett*. 2000;293(1):49–52.
41. Beck K, et al. Interplay between heme oxygenase-1 and the multifunctional transcription factor yin yang 1 in the inhibition of intimal hyperplasia. *Circ Res*. 2010;107(12):1490–1497.
42. Collinson EJ, et al. The yeast homolog of heme oxygenase-1 affords cellular antioxidant protection via the transcriptional regulation of known antioxidant genes. *J Biol Chem*. 2011;286(3):2205–2214.
43. Lin Q, et al. Heme oxygenase-1 protein localizes to the nucleus activates transcription factors important in oxidative stress. *J Biol Chem*. 2007;282(28):20621–20633.
44. Lin QS, Weis S, Yang G, Zhuang T, Abate A, Dennery PA. Catalytic inactive heme oxygenase-1 protein regulates its own expression in oxidative stress. *Free Radic Biol Med*. 2008;44(5):847–855.
45. Basuroy S, et al. HO-2 provides endogenous protection against oxidative stress apoptosis caused by TNF-alpha in cerebral vascular endothelial cells. *Am J Physiol Cell Physiol*. 2006;291(5):C897–C908.
46. Chang EF, et al. Heme oxygenase-2 protects against lipid peroxidation-mediated cell loss impaired motor recovery after traumatic brain injury. *J Neurosci*. 2003;23(9):3689–3696.
47. Zakhary R, Poss KD, Jaffrey SR, Ferris CD, Tonegawa S, Snyder SH. Targeted gene deletion of heme oxygenase 2 reveals neural role for carbon monoxide. *Proc Natl Acad Sci U S A*. 1997;94(26):14848–14853.
48. King JT Jr. Epidemiology of aneurysmal subarachnoid hemorrhage. *Neuroimaging Clin N Am*. 1997;7(4):659–668.
49. Rincon F, Rossenwasser RH, Dumont A. The epidemiology of admissions of nontraumatic subarachnoid hemorrhage in the United States. *Neurosurgery*. 2013;73(2):217–222.
50. Hijdra A, Van Gijn J, Stefanko S, Van Dongen KJ, Vermeulen M, Van Crevel H. Delayed cerebral ischemia after aneurysmal subarachnoid hemorrhage: clinicoanatomic correlations. *Neurology*. 1986;36(3):329–333.
51. Kassell NF, Torner JC, Haley EC Jr, Jane JA, Adams HP, Kongable GL. The International Cooperative Study on the Timing of Aneurysm Surgery. Part 1: Overall management results. *J Neurosurg*. 1990;73(1):18–36.
52. Rosengart AJ, et al. Outcome in patients with subarachnoid hemorrhage treated with antiepileptic drugs. *J Neurosurg*. 2007;107(2):253–260.
53. Fergusen S, Macdonald RL. Predictors of cerebral infarction in patients with aneurysmal subarachnoid hemorrhage. *Neurosurgery*. 2007;60(4):658–667.
54. Macdonald RL, et al. Clazosentan to overcome neurological ischemia and infarction occurring after subarachnoid hemorrhage (CONSCIOUS-1): randomized, double-blind, placebo-controlled phase 2 dose-finding trial. *Stroke*. 2008;39(11):3015–3021.
55. Vergouwen MD, Ilodigwe D, Macdonald RL. Cerebral infarction after subarachnoid hemorrhage contributes to poor outcome by vasospasm-dependent and -independent effects. *Stroke*. 2011;42(4):924–929.
56. Iadecola C, Anrather J. The immunology of stroke: from mechanisms to translation. *Nat Med*. 2011;17(7):796–808.
57. Macdonald RL. Delayed neurological deterioration after subarachnoid haemorrhage. *Nat Rev Neurol*. 2014;10(1):44–58.
58. Hanafy KA. The role of microglia and the TLR4 pathway in neuronal apoptosis vasospasm after subarachnoid hemorrhage. *J Neuroinflammation*. 2013;10:83.
59. Vinet J, et al. Neuroprotective function for ramified microglia in hippocampal excitotoxicity. *J Neuroinflammation*. 2012;9:27.
60. Montero M, Gonzalez B, Zimmer J. Immunotoxic depletion of microglia in mouse hippocampal slice cultures enhances ischemia-like neurodegeneration. *Brain Res*. 2009;1291:140–152.
61. Boscia F, Esposito CL, Di Crisci A, de Franciscis V, Annunziato L, Cerchia L. GDNF selectively induces microglial activation and neuronal survival in CA1/CA3 hippocampal regions exposed to NMDA insult through Ret/ERK signalling. *PLoS One*. 2009;4(8):e6486.
62. Ajami B, Bennett JL, Krieger C, Tetzlaff W, Rossi FM. Local self-renewal can sustain CNS microglia maintenance and function throughout adult life. *Nat Neurosci*. 2007;10(12):1538–1543.
63. Soulet D, Rivest S. Bone-marrow-derived microglia: myth or reality? *Curr Opin Pharmacol*. 2008;8(4):508–518.
64. Kristiansen M, et al. Identification of the haemoglobin scavenger receptor. *Nature*. 2001;409(6817):198–201.
65. Zhao X, et al. Hematoma resolution as a target for intracerebral hemorrhage treatment: role for peroxisome proliferator-activated receptor gamma in microglia/macrophages. *Ann Neurol*. 2007;61(4):352–362.
66. Figueiredo RT, et al. Characterization of heme as activator of Toll-like receptor 4. *J Biol Chem*. 2007;282(28):20221–20229.

67. D'Amico G, Lam F, Hagen T, Moncada S. Inhibition of cellular respiration by endogenously produced carbon monoxide. *J Cell Sci*. 2006;119(pt 11):2291–2298.
68. Wegiel B, et al. Heme oxygenase-1 derived carbon monoxide permits maturation of myeloid cells. *Cell Death Dis*. 2014;5:e1139.
69. Smith A, Wu AH, Lynch KL, Ko N, Grenache DG. Multi-wavelength spectrophotometric analysis for detection of xanthochromia in cerebrospinal fluid and accuracy for the diagnosis of subarachnoid hemorrhage. *Clin Chim Acta*. 2013;424:231–236.
70. Jung S, et al. Analysis of fractalkine receptor CX(3)CR1 function by targeted deletion green fluorescent protein reporter gene insertion. *Mol Cell Biol*. 2000;20(11):4106–4114.
71. Imai T, et al. Identification and molecular characterization of fractalkine receptor CX3CR1, which mediates both leukocyte migration adhesion. *Cell*. 1997;91(4):521–530.
72. Fong AM, et al. Fractalkine and CX3CR1 mediate a novel mechanism of leukocyte capture, firm adhesion, activation under physiologic flow. *J Exp Med*. 1998;188(8):1413–1419.
73. Foussat A, et al. Fractalkine receptor expression by T lymphocyte subpopulations and in vivo production of fractalkine in human. *Eur J Immunol*. 2000;30(1):87–97.
74. Tong N, et al. Neuronal fractalkine expression in HIV-1 encephalitis: roles for macrophage recruitment neuroprotection in the central nervous system. *J Immunol*. 2000;164(3):1333–1339.
75. Harrison JK, et al. Role for neuronally derived fractalkine in mediating interactions between neurons and CX3CR1-expressing microglia. *Proc Natl Acad Sci U S A*. 1998;95(18):10896–10901.